

Universality and Diversity of Solar Winds Driven by Nonlinear Low-Frequency Alfvén Waves from the Photosphere -Fast/Slow Winds and Disappearance of Solar Winds-

Takeru K. Suzuki¹ & Shu-ichiro Inutsuka

Department of Physics, Kyoto University, Kitashirakawa, Kyoto, 606-8502, Japan

Abstract. We investigate how the properties of the corona and solar wind in the open coronal holes depend on the properties of the magnetic fields and their footpoint motions at the surface. We perform one-dimensional magnetohydrodynamical (MHD) simulations for the heating and the acceleration in the coronal holes by low-frequency Alfvén waves from the photosphere to 0.3 or 0.1AU. We impose low-frequency ($\lesssim 0.05\text{Hz}$) transverse fluctuations of the field lines at the photosphere with various amplitude, spectrum, and polarization in the open flux tubes with different photospheric field strength, $B_{r,0}$, and super-radial expansion of the cross section, f_{max} . We find that a transonic solar wind is the universal consequence. The atmosphere is also stably heated up to $\gtrsim 10^6\text{K}$ by the dissipation of the Alfvén waves through compressive-wave generation and wave reflection in the case of the sufficient wave input with photospheric amplitude, $\langle dv_{\perp,0} \rangle \gtrsim 0.7\text{km s}^{-1}$. The density, and accordingly the mass flux, of solar winds show a quite sensitive dependence on $\langle dv_{\perp,0} \rangle$ because of an unstable aspect of the heating by the nonlinear Alfvén waves. A case with $\langle dv_{\perp,0} \rangle = 0.4\text{km s}^{-1}$ gives $\simeq 50$ times smaller mass flux than the fiducial case for the fast wind with $\langle dv_{\perp,0} \rangle = 0.7\text{km s}^{-1}$; solar wind *almost disappears* only if $\langle dv_{\perp,0} \rangle$ becomes \simeq half. We also find that the solar wind speed has a positive correlation with $B_{r,0}/f_{\text{max}}$, which is consistent with recent observations by Kojima et al. Based on these findings, we show that both fast and slow solar winds can be explained by the single process, the dissipation of the low-frequency Alfvén waves, with different sets of $\langle dv_{\perp,0} \rangle$ and $B_{r,0}/f_{\text{max}}$. Our simulations naturally explain the observed (i) anticorrelation of the solar wind speed and the coronal temperature and (ii) larger amplitude of the Alfvénic fluctuations in the fast winds. In Appendix, we also explain our implementation of the outgoing boundary condition of the MHD waves with some numerical tests.

1. Introduction

The corona can be roughly divided into two sectors with respect to the magnetic field configurations on the solar surface. One is closed field regions in which both footpoints of each field line are rooted at the photosphere. The other is open field regions in which one footpoint is anchored at the photosphere and the other is open into the interplanetary space. The open field regions roughly coincide with the area called coronal holes which are dark in X-rays. From the coronal holes, the hot plasma streams out as solar winds.

The Alfvén wave, generated by the granulations or other surface activities, are a promising candidate operating in the heating and acceleration of the solar winds from the coronal holes. It can travel a long distance so that the dissipation plays a role in the heating of the solar wind plasma as well as the lower coronal plasma, in contrast to other processes, such as magnetic reconnection events and compressive waves, the heating of which probably concentrates at lower altitude. The high-frequency ($\sim 10^4\text{Hz}$) ioncyclotron waves are recently attracted for the preferential heating of the perpendicular temperature of the heavy ions [Kohl et al., 1998]. However, the protons which compose the main part of the plasma are supposed to be mainly heated by the low-frequency ($\lesssim 0.1\text{Hz}$) components in the magnetohydrodynamical (MHD) regime. This is firstly because the low-frequency waves are expected to have more power, and secondly because the resonance frequency of the protons is higher than

that of heavier ions so that the energy of the ioncyclotron waves is in advance absorbed by the heavy ions [Cranmer, 2000].

The treatment of the wave dissipation is quite complicated even for the MHD processes. The main reason is that the nonlinearity becomes essential because amplitudes of upgoing waves are inevitably amplified in the stratified atmosphere with decreasing density. Therefore, numerical simulation is a powerful tool; there are several works on the wave propagation and dissipation [Kudoh & Shibata, 1999; Ofman & Davila, 1998; Orta et al., 2003; Ofman, 2004]. However, large density contrast amounting more than 15 orders of magnitude from the photosphere to the outer heliosphere has prevented one from carrying out numerical simulation in the broad region from the photosphere to the interplanetary space even in one-dimensional (1D) modeling.

In Suzuki & Inutsuka [2005] (paper I hereafter) we successfully carried out 1D MHD simulation with radiative cooling and thermal conduction from the photosphere to 0.3 AU. We showed that the coronal heating and the fast solar wind acceleration in the coronal holes are natural consequence of the transverse footpoint fluctuations of the magnetic field lines. The low-frequency ($\lesssim 0.05\text{Hz}$) Alfvén waves are generated by the photospheric fluctuations. The sufficient amount of their energy transmits into the corona in spite of the attenuation in the chromosphere and the transition region (TR), so that they effectively dissipate to heat and accelerate the coronal plasma. Although it is based on the one-fluid MHD approximation (§6.2), it, for the first time, self-consistently treats the plasma heating and the propagation of the Alfvén waves from the photosphere to the interplanetary space. However, we studied the only one case for the fast solar wind in paper I. It is important to examine how our result is universal and the properties of the corona and the solar wind are affected by adopting different types of the

¹JSPS Research Fellow

wave injections and/or different magnetic field geometry of the flux tubes. The purpose of this paper is to study the universality of the heating by the low-frequency Alfvén waves.

In this paper we adopt the one-fluid MHD approximation in 1D flux tubes, which is the same as in paper I. This assumption is not strictly correct in the solar wind plasma, which will be discussed later (§6.2). However, we think that the MHD approximation is still appropriate for the studies of the average properties of the main part of the plasma, namely the protons. This is because the Larmor radii of the ions due to the fluctuation of the field lines, B_{\perp} , are smaller than the shortest wavelength we are considering (waves with a period 20s) in the entire regions. Therefore, the particles of each component can be sufficiently randomized by the fluctuating magnetic fields.

2. Simulation Set-up

We consider 1D open flux tube which is super-radially open, measured by heliocentric distance, r . The simulation region is from the photosphere ($r = 1R_{\odot}$) with density, $\rho = 10^{-7} \text{g cm}^{-3}$, to $65R_{\odot}$ (0.3AU) or $\simeq 20R_{\odot}$ ($\simeq 0.1\text{AU}$), where R_{\odot} is solar radius. Radial field strength, B_r , is given by conservation of magnetic flux as

$$B_r r^2 f(r) = \text{const.}, \tag{1}$$

where $f(r)$ is super-radial expansion factor. We adopt the same function as in Kopp & Holzer [1976] for $f(r)$ but consider two-step expansions:

$$f(r) = \frac{f_{1,\text{max}} \exp(\frac{r-R_1}{\sigma_1}) + f_1}{\exp(\frac{r-R_1}{\sigma_1}) + 1} \frac{f_{2,\text{max}} \exp(\frac{r-R_2}{\sigma_2}) + f_2}{\exp(\frac{r-R_2}{\sigma_2}) + 1}$$

where $f_1 = 1 - (f_{1,\text{max}} - 1) \exp(\frac{R_{\odot}-R_1}{\sigma_1})$ and $f_2 = 1 - (f_{2,\text{max}} - 1) \exp(\frac{R_{\odot}-R_2}{\sigma_2})$. The flux tube initially expands by a factor of $f_{1,\text{max}}$ around $R_1 = 1.01R_{\odot}$ corresponding to the 'funnel' structure [Tu et al., 2005], and followed by $f_{2,\text{max}}$ times expansion around $R_2 = 1.2R_{\odot}$ due to the large scale dipole magnetic fields (Figure 1). We define the total super-radial expansion as $f_{\text{max}} = f_{1,\text{max}} f_{2,\text{max}}$.

We give transverse fluctuations of the field line by the granulations at the photosphere, which excite Alfvén waves. We study cases of various spectra, polarizations, and root mean squared (rms) amplitudes, $\langle dv_{\perp,0} \rangle (\equiv \sqrt{\langle dv_{\perp,0}^2 \rangle}) (\text{km s}^{-1})$. $\langle dv_{\perp,0} \rangle$ and power spectrum, $P(\nu) (\text{erg g}^{-1} \text{Hz}^{-1})$, have a relation of

$$\langle dv_{\perp,0}^2 \rangle = \int_{\nu_{\text{low cut}}^{\text{up}}}^{\nu_{\text{up cut}}^{\text{up}}} P(\nu) d\nu. \tag{2}$$

The parameters adopted in different simulation Runs are tabulated in Table 1. We consider three types of spectrum : (i) $P(\nu) \propto \nu^{-1}$ (ii) $P(\nu) \propto \nu^0$ (white noise) (iii) $P(\nu) \propto \delta(1/\nu - 180\text{s})$ (sinusoidal waves with a period of 180 seconds) . For the first and second cases we set $\nu_{\text{low cut}} = 6 \times 10^{-4} \text{Hz}$ (period of $\simeq 30\text{min}$) and $\nu_{\text{up cut}} = 0.05 \text{Hz}$ (20s) for Run I or $\nu_{\text{up cut}} = 0.025 \text{Hz}$ (40s) for the others. For the linearly polarized perturbations we only take into account one transverse component besides the radial component, while we consider the two transverse components for the circularly polarized case. The values of $\langle dv_{\perp,0} \rangle$ are chosen to be compatible with the observed photospheric velocity amplitude $\sim 1 \text{km s}^{-1}$ [Holweger et al., 1978]. At the outer boundary, non-reflecting condition is imposed for all the MHD waves (see Appendix), which enables us to carry out simulations for a long time until quasi-steady state behaviors are achieved without unphysical wave reflection.

Table 1. Model Parameters

run	I	II	III	IV	V	VI	VII	VIII	IX	X
Outer Bound.	$65R_{\odot}$	$20R_{\odot}$	$20R_{\odot}$	$20R_{\odot}$	$20R_{\odot}$	$20R_{\odot}$	$20R_{\odot}$	$22R_{\odot}$	$20R_{\odot}$	$65R_{\odot}$
Spectrum	ν^{-1}	ν^{-1}	ν^0	$\delta(\nu^{-1} - 180\text{s})$	$\delta(\nu^{-1} - 180\text{s})$	ν^{-1}	ν^{-1}	ν^{-1}	ν^{-1}	ν^{-1}
Polarization	Linear	Linear	Linear	Linear	Circular	Linear	Linear	Linear	Linear	Linear
$\langle dv_{\perp,0} \rangle (\text{km/s})$	0.7	0.7	0.7	0.7	0.7	1.4	0.4	0.7	0.3	1.0
$B_{r,0} (\text{G})$	161	161	161	161	161	161	161	322	161	322
$f_{1,\text{max}}$	30	30	30	30	30	30	30	45	30	45
$f_{2,\text{max}}$	2.5	2.5	2.5	30	2.5	2.5	2.5	10	2.5	10
Description	Fast Wind (paper I)	Coarse Ver. of run I							No Steady State	Slow Wind

We dynamically treat the propagation and dissipation of the waves and the heating and acceleration of the plasma by solving ideal MHD equations with the relevant physical processes (paper I):

$$\frac{d\rho}{dt} + \frac{\rho}{r^2 f} \frac{\partial}{\partial r} (r^2 f v_r) = 0, \quad (3)$$

$$\begin{aligned} \rho \frac{dv_r}{dt} = & -\frac{\partial p}{\partial r} - \frac{1}{8\pi r^2 f} \frac{\partial}{\partial r} (r^2 f B_\perp^2) \\ & + \frac{v_\perp^2}{2r^2 f} \frac{\partial}{\partial r} (r^2 f) - \rho \frac{GM_\odot}{r^2}, \end{aligned} \quad (4)$$

$$\rho \frac{d}{dt} (r\sqrt{f}v_\perp) = \frac{B_r}{4\pi} \frac{\partial}{\partial r} (r\sqrt{f}B_\perp). \quad (5)$$

$$\begin{aligned} \rho \frac{d}{dt} \left(e + \frac{v^2}{2} + \frac{B^2}{8\pi\rho} \right) + \frac{1}{r^2 f} \frac{\partial}{\partial r} [r^2 f \{ (p + \frac{B^2}{8\pi}) v_r - \frac{B_r}{4\pi} (\mathbf{B} \cdot \mathbf{v}) \}] \\ + \frac{1}{r^2 f} \frac{\partial}{\partial r} (r^2 f F_c) + q_R = 0, \end{aligned} \quad (6)$$

$$\frac{\partial B_\perp}{\partial t} = \frac{1}{r\sqrt{f}} \frac{\partial}{\partial r} [r\sqrt{f}(v_\perp B_r - v_r B_\perp)], \quad (7)$$

where ρ , \mathbf{v} , p , \mathbf{B} are density, velocity, pressure, and magnetic field strength, respectively, and subscript r and \perp denote radial and tangential components; $\frac{d}{dt}$ and $\frac{\partial}{\partial t}$ denote Lagrangian and Eulerian derivatives, respectively; $e = \frac{1}{\gamma-1} \frac{p}{\rho}$ is specific energy and we assume the equation of state for ideal gas with a ratio of specific heat, $\gamma = 5/3$; G and M_\odot are the gravitational constant and the solar mass; F_c is thermal conductive flux and q_R is radiative cooling. We use optically thin radiative loss [Landini & Monsignori-Fossi, 1990] in the corona and upper TR where temperature, $T \geq 4 \times 10^4 \text{K}$. In the chromosphere and low TR, we adopt empirical radiative cooling based on the observations [Anderson & Athay, 1989; Moriyasu et al., 2004] to take into account the optically thick effect. In the low chromosphere, the temperature sometimes drops to $\sim 3000 \text{K}$ because we do not consider other heating sources, such as sound waves, which must be important there besides Alfvén waves [Bogdan et al., 2003]. Such unrealistically low temperature interrupts the propagation of the Alfvén waves in the low chromosphere through the change of the density structure. To give realistic estimates of the transmission of the Alfvén waves there, we switch off the radiative cooling, if the temperature becomes $< 5000 \text{K}$ only when $\rho > 10^{-11} \text{g cm}^{-3}$.

We adopt the second-order MHD-Godunov-MOCCT scheme (Sano & Inutsuka 2005) to update the physical quantities. We solve eqs. (3)–(6) on fixed Eulerian mesh by remapping the physical variables updated in Lagrangian coordinate onto the original grids at each time step. The induction equation (7) is solved on the Eulerian grids. We use implicit time step for the thermal conduction and radiative cooling in energy eq.(6) because the Courant conditions are severe for these processes, while explicit time step is adopted for the other terms. A great advantage of our code is that no artificial viscosity is required even for strong MHD shocks

because we solve the non-linear Riemann problem by taking into account the magnetic pressure at each cell boundary.

We initially set static atmosphere with temperature $T = 10^4 \text{K}$ to see whether the atmosphere is heated up to coronal temperature and accelerated to accomplish the transonic flow. At $t = 0$ we start to inject the transverse fluctuations from the photosphere and continue the simulations until the quasi-steady states are achieved.

3. Heating and Acceleration by Wave Dissipation

Before showing the results of the various coronal holes, we explain how the coronal heating and the solar wind acceleration were accomplished in the fiducial case (Run I) which was studied in paper I for the fast solar wind. Figure 2 plots the initial condition (dashed lines) and the results after the quasi-steady state condition is achieved at $t = 2573$ minutes (solid lines) in Run I, compared with the recent observations of fast solar winds. From top to bottom, v_r (km s^{-1}), T (K), mass density, ρ (g cm^{-3}), and rms transverse amplitude, $\langle dv_\perp \rangle$ (km s^{-1}) are plotted. As for the density, we compare our result with observed electron density, N_e , in the corona. When deriving N_e from ρ in the corona, we assume fully ionized H & He, and $N_e (\text{cm}^{-3}) = 10^{24} \rho (\text{g cm}^{-3})$. These variables are averaged for 3 minutes to incorporate observational exposure time.

Figure 2 shows that the initial cool and static atmosphere is effectively heated and accelerated by the dissipation of the Alfvén waves. The sharp TR which divides the cool chromosphere with $T \sim 10^4 \text{K}$ and the hot corona with $T \sim 10^6 \text{K}$ is formed due to the thermally unstable region around $T \sim 10^5 \text{K}$ in the radiative cooling function [Landini & Monsignori-Fossi, 1990]. The hot corona streams out as the transonic solar wind. The simulation naturally explains the observed trend quite well. (see paper I for more detailed discussions.)

Figure 3 shows transfer of the energy (upper) and momentum (lower) flux of various components described below. The energy equation in an Eulerian form becomes

$$\frac{\partial E}{\partial t} + \nabla \cdot \mathbf{F} + L_{\text{loss}} = 0,$$

where E and \mathbf{F} are the total energy density and flux. $-L_{\text{loss}}$ is loss of the energy. For the analyses of the quasi-steady state behaviors, we can reasonably assume that the first term equals to 0. Then, in our case the explicit form becomes

$$\begin{aligned} \frac{1}{r^2 f} \frac{\partial}{\partial r} [r^2 f \{ \rho v_r (\frac{v_r^2 + v_\perp^2}{2} + e + \frac{p}{\rho} - \frac{GM_\odot}{r}) \\ + \frac{B_\perp^2}{4\pi} v_r - \frac{B_r B_\perp v_\perp}{4\pi} + F_c \}] + q_R = 0. \end{aligned} \quad (8)$$

Using the relation, $v_\perp = -B_\perp / \sqrt{4\pi\rho}$, for the outgoing Alfvén waves, we can extract the energy flux of the Alfvén waves from eq.(8) as follows [Jacques, 1977]:

$$\begin{aligned} \langle F_A \rangle = \langle \rho v_\perp^2 (v_A + v_r) + p_A v_r \rangle = \langle -\frac{B_r B_\perp v_\perp}{4\pi} \rangle \\ + \langle (\frac{\rho v_\perp^2}{2} + \frac{B_\perp^2}{8\pi}) v_r \rangle + \langle \frac{B_\perp^2}{8\pi} v_r \rangle, \end{aligned} \quad (9)$$

where $\langle \rangle$ denotes the time-average and we define Alfvén wave pressure as $p_A = B_\perp^2/8\pi$. In the upper panel of Figure 3 we plot the wave energy flux, $\langle F_A \rangle \frac{r^2 f(r)}{r_c^2 f(r_c)}$, normalized by cross section of the flux tube at $r_c = 1.02R_\odot$ with kinetic energy flux, $\rho v_r \frac{v_r^2}{2} \frac{r^2 f(r)}{r_c^2 f(r_c)}$, enthalpy flux, $\rho v_r (e + \frac{p}{\rho}) \frac{r^2 f(r)}{r_c^2 f(r_c)}$, and integrated radiative loss, $\int_{R_\odot}^r q_R \frac{r^2 f(r)}{r_c^2 f(r_c)} dr$. While the most of the initial wave energy escapes by the radiation loss in the chromosphere and the low corona, the remained energy, which is $\sim 10\%$ of the input, is transferred to the kinetic energy of the solar wind in the outer region. The thermal energy is almost constant in the corona, which indicates that the $\sim 1\text{MK}$ plasma is maintained by the energy balance among the wave heating, the radiative cooling, adiabatic cooling (solar wind acceleration), and the redistribution by the thermal conduction.

The lower panel of Figure 3 plots measure of the pressure of the Alfvén waves, $\langle p_A v_r \rangle$, and thermal gas, $\langle p v_r \rangle$. This shows that the Alfvén wave pressure dominates the gas pressure in the solar wind acceleration region ($1.5R_\odot \lesssim r \lesssim 10R_\odot$); the fast solar wind is driven by the wave pressure rather than by the thermal pressure.

In paper I, we claimed that the dissipation of the low-frequency Alfvén waves in the corona is mainly by the generation of the slow waves and the reflection of the Alfvén waves due to the density fluctuation of the slow modes. This can be seen in $r - t$ diagrams. Figure 4 presents contours of amplitude of v_r , ρ , v_\perp , and B_\perp/B_r in $R_\odot \leq r \leq 15R_\odot$ from $t = 2570$ min. to 2600 min. Dark (light) shaded regions denote positive (negative) amplitude. Above the panels, we indicate the directions of the local 5 characteristics, two Alfvén, two slow, and one entropy waves at the respective positions. Note that the fast MHD and Alfvén modes degenerate in our case (wave vector and underlying magnetic field are in the same direction), so we simply call the innermost and outermost waves Alfvén modes. In our simple 1D geometry, v_r and ρ trace the slow modes which have longitudinal wave components, while v_\perp and B_\perp trace the Alfvén modes which are transverse (see Cho & Lazarian [2002;2003] for more general cases.).

One can clearly see the Alfvén waves in v_\perp and B_\perp/B_r diagrams, which have the same slopes with the Alfvén characteristics shown above. One can also find the incoming modes propagating from lower-right to upper-left as well as the outgoing modes generated from the surface¹. These incoming waves are generated by the reflection at the ‘density mirrors’ of the slow modes. At intersection points of the outgoing and incoming characteristics the non-linear wave-wave interactions take place, which play a role in the wave dissipation.

The slow modes are seen in v_r and ρ diagrams. Although it might be difficult to distinguish, the most of the patterns are due to the outgoing slow modes² which are generated from the perturbations of the Alfvén wave pressure, $B_\perp^2/8\pi$

[Kudoh & Shibata, 1999; Tsurutani et al., 2002]. These slow waves steepen eventually and lead to the shock dissipation.

The processes discussed here are the combination of the direct mode conversion to the compressive waves and the parametric decay instability due to three-wave (outgoing Alfvén, incoming Alfvén, and outgoing slow waves) interactions (Goldstein 1978; Terasawa et al. 1986; see also §4.1.2) of the Alfvén waves. Although they are not generally efficient in the homogeneous background since they are the nonlinear mechanisms, the density gradient of the background plasma totally changes the situation in our simulation. The density rapidly decreases in the corona owing to the gravity as r increases, which results in the amplification of the wave amplitude so that the waves easily become nonlinear. Furthermore, the Alfvén speed varies a lot due to the change of the density even within one wavelength of Alfvén waves with periods of minutes or longer. This leads to both variation of the wave pressure in one wavelength and partial reflection through the deformation of the wave shape [Moore et al., 1991]. The dissipation is greatly enhanced by the density stratification, in comparison with the case of the homogeneous background. Thus, the low-frequency Alfvén waves are effectively dissipated, which results in the heating and acceleration of the coronal plasma.

In summarize, we have shown that the low-frequency Alfvén waves are dissipated via the combination of the direct mode conversion and the decay instability which are considerably enhanced by the long wavelength (so called “non-WKB”) effect in the stratified atmosphere. Although each process is not individually effective enough, the suitable dissipation rate is realized by the combination.

4. Universality and Diversity

We investigate how the properties of the corona and solar wind depend on the parameters of the input photospheric fluctuations and the flux tube geometry. We use smaller simulation boxes in Run II-IX than in Run I (Table 1) to save the computational time for the parameter studies. In most cases quasi-steady state conditions are achieved after $t \gtrsim 1800$ min. In this section we show results at $t = 2900$ min unless explicitly stated.

4.1. Various Input Waves

4.1.1. Wave Spectrum

We show the dependence on the spectrum, $P(\nu)$, of the photospheric fluctuations. We here compare the results of $P(\nu) \propto \nu^{-1}$ (Run II), ν^0 (white noise; Run III), and purely sinusoidal perturbation with a period of 180 s, $P(\nu) \propto \delta(\nu^{-1} - 180\text{s})$ (Run IV). Figure 5 shows structure of the coronae and solar winds. The upper panel of Figure 6 plots adiabatic constant, S_c , of the outgoing Alfvén waves derived from wave action [Jacques, 1977]:

$$S_c = \rho \delta v_{A,+}^2 \frac{(v_r + v_A)^2}{v_A} \frac{r^2 f(r)}{r_c^2 f(r_c)}, \quad (10)$$

where

$$\delta v_{A,+} = v_\perp - B_\perp / \sqrt{4\pi\rho} \quad (11)$$

is amplitude of the outgoing Alfvén waves (Elsässer variables). The lower panel shows nonlinearity, $\delta v_{A,+}/v_A$ of the outgoing Alfvén waves.

Figure 5 shows that the plasma is heated up to the coronal temperature and accelerated to 400-600km/s at 0.1AU in all the Runs. Particularly, the results of $P(\nu) = \nu^{-1}$ and ν^0 are quite similar. The attenuation of the outgoing Alfvén waves is due to the two kinds of the processes, the shocks and the reflection in our simulations. The shock dissipation per unit distance is larger for waves with larger ν because the number of shocks is proportional to wavenumber. On the other hand, Alfvén waves with smaller ν suffer the reflection more since the wavelengths are relatively larger against the variation scale of the Alfvén speed so that the wave shapes are deformed more. These two ingredients with respect to the ν dependence cancel in these two cases, and variations of the energy and the amplitude become quite similar (Figure 6). The structures of the corona and the solar wind are also similar since they are the consequence of the wave dissipation.

The results of the purely sinusoidal fluctuation (Run IV) is slightly different from the other two cases. The TR is not so sharp as those in the other two Runs. The temperature firstly rises at $r - R_\odot = 0.005R_\odot$, but drops slightly and again rises around $r - R_\odot = 0.02R_\odot$. Actually, the TR moves back and forth more compared to the other cases. This is because the shock heating takes place rather intermittently only at the wave crests in the sinusoidal case, while in the other cases the heating is distributed more uniformly by the contributions from waves with various ν . As a result, the chromospheric evaporation occurs intermittently so that the TR becomes dynamical. The sharpness of the TR is important in terms of the wave reflection. In the sinusoidal case (Run IV) the Alfvén waves becomes more transparent at the TR since the variation of the Alfvén speed is more gradual. Therefore, more wave energy transmits into the corona, avoiding the reflection at the TR (Figure 6). Accordingly, the temperature and density in the outer region become higher owing to the larger plasma heating (Figure 5).

4.1.2. Wave Polarization

We examine the effect of the wave polarization. Linearly polarized Alfvén waves dissipate by the direct steepening [Hollweg, 1982; Suzuki, 2004] to MHD fast shocks as well as by the parametric decay instability [Goldstein, 1978]. On the other hand, circularly polarized components do not steepen, and it dissipates only by the parametric decay instability in our one-fluid MHD framework, so that the dissipation becomes less efficient.

Figures 7 and 8 compare the results of the sinusoidal linearly polarized (Run IV) and circularly polarized (Run V) fluctuations. The results of Run II are also plotted for comparison. It is shown that the coronal heating and solar wind acceleration are still achieved by the dissipation of the circularly polarized Alfvén waves (Figure 7) although more wave energy is remained at the outer boundary (Figure 8) due to the less dissipative character.

A key ingredient for the efficient dissipation is the rapid decrease of the density owing to the gravity as discussed in

§3. The circularly polarized Alfvén waves which are initially sinusoidal are quickly deformed by the rapid variation of the density in the chromosphere and the low corona; simple sinusoidal waves cannot propagate any further unless the wavelengths are sufficiently short. As a result, the incoming Alfvén waves are generated by the shape deformation. The compressive slow waves are also easily generated even without the steepening because the variation of the magnetic pressure is present because of the large difference of the Alfvén speed within one wavelength.

It has been generally believed that the decay instability of the Alfvén waves is not important in the context of the coronal heating and the solar wind acceleration. However, our simulation shows that this is not the case; the three-wave interactions are greatly enhanced by the long wavelength effect so that the sufficient wave dissipation occurs in the real solar corona.

The case of the circularly polarized waves give smaller coronal density and temperature since the wave dissipation is less effective. However, the solar wind speed is rather faster, up to 700km/s at 0.1AU, because the less dense plasma can be efficiently accelerated.

4.1.3. Wave Amplitude

We study dependences on the amplitudes of the input fluctuations at the photosphere. We compare the results of larger $\langle dv_{\perp,0} \rangle = 1.4\text{km s}^{-1}$ (Run VI) and smaller $\langle dv_{\perp,0} \rangle = 0.4\text{km s}^{-1}$ (Run VII) cases with the fiducial case ($\langle dv_{\perp,0} \rangle = 0.7\text{km s}^{-1}$; Run II) in Figures 9 and 10. We also show the results of $\langle dv_{\perp,0} \rangle = 0.3\text{km s}^{-1}$ (Run IX) at $t = 1100\text{min}$ in Figure 9, although the quasi steady-state behavior is not achieved. At later epochs in Run IX, the density and temperature decrease with time as explained later.

The maximum temperature of Run VII ($\langle dv_{\perp,0} \rangle = 0.4\text{km/s}$) is $\simeq 5 \times 10^5\text{K}$, which is cooler than the usual corona. The density is much lower than the fiducial case by 1-2 orders of magnitude because the sufficient mass cannot supply into the corona by the chromospheric evaporation, owing to the low temperature. As a result, the mass flux (ρv_r) becomes more than an order of magnitude lower than that of the present solar wind, although the outflow velocity ($\sim 1000\text{km/s}$ at 0.1AU) is slightly faster than the present value. These tendencies are more extreme in Run IX; the temperature is about $2 \times 10^5\text{K}$ and the density in the corona and solar wind is smaller by 3 orders of magnitude than the fiducial case.

This behavior can be understood by the wave dissipation (Figure 10). The input wave energy ($\propto \langle dv_{\perp,0}^2 \rangle$) in Run VII is 1/3 of that of Run II. However, the upper panel of Figure 10 shows that the remained S_c 's in both cases are similar at 0.1AU, which indicates that the Alfvén waves do not effectively dissipate in the smaller $\langle dv_{\perp,0} \rangle$ case. This is because the Alfvén speed ($= B/\sqrt{4\pi\rho}$) is larger due to the lower density and the nonlinearity, $\delta v_{A,+}/v_A$, becomes weaker. As a result, the final energy flux of the solar wind at 0.1AU, mostly consisting of the kinetic energy ($\rho v_r \frac{v_r^2}{2}$), becomes one order of magnitude smaller although the ratio of the input wave energy is only 1/3.

Once the coronal density starts to decrease, a positive feedback operates. Namely, a decrease of the density leads to weaker non-linearity of the Alfvén waves, which reduces the plasma heating by the wave dissipation. This decreases the coronal temperature, and further reduces the coronal density by the suppression of the chromospheric evaporation. This takes place in Run IX ($\langle dv_{\perp,0} \rangle = 0.3 \text{ km s}^{-1}$) so that the coronal density and temperature continue to decrease at later epochs, instead of maintaining steady corona and solar wind.

Our results show that $\langle dv_{\perp,0} \rangle \gtrsim 0.4 \text{ km s}^{-1}$ is the criterion of the photospheric fluctuations for the formation of the stable hot plasma. To get the maximum coronal temperature $\gtrsim 10^6 \text{ K}$, $\langle dv_{\perp,0} \rangle \gtrsim 0.7 \text{ km s}^{-1}$ is required. Otherwise if $\langle dv_{\perp,0} \rangle \lesssim 0.3 \text{ km s}^{-1}$, the low-frequency Alfvén waves cannot maintain the hot corona, and the solar wind mass flux becomes drastically small; the solar winds *virtually disappear* (see §4.1.4).

Larger $\langle dv_{\perp,0} \rangle$ gives larger coronal density as shown in Run VI. The initial increase of the temperature starts from deeper location around $r \simeq 0.005 R_{\odot}$ than the other cases. Thanks to this, a decrease of the density is slower (larger pressure scale height) so that the density around $r = 1.01 R_{\odot}$ is two orders of magnitude larger than that of Run II. However, the temperature decreases slightly instead of a monotonical increase; it cannot go over the peak of the radiative cooling function at $T \simeq 10^5 \text{ K}$ [Landini & Monsignori-Fossi, 1990] because the radiative loss is efficient owing to the large density. The second increase of the temperature begins from $r \simeq 1.03 R_{\odot}$ and above that the corona is formed. The coronal density and temperature are larger than those in Run II. In particular the density in the outer region is 10 times larger, and the mass flux of the solar wind is larger by the same extent. The top panel of Figure 10 shows that the Alfvén waves dissipate more effectively in the larger $\langle dv_{\perp,0} \rangle$ case. The reason is the same as that explained for the smaller $\langle dv_{\perp,0} \rangle$ cases; the nonlinearity, $\delta v_{A,+}/v_A$, of the Alfvén waves becomes larger because $\delta v_{A,+}$ itself is larger and v_A is smaller owing to the larger density.

Figure 11 summarizes the maximum coronal temperature, $T_{\text{max}}(\text{K})$ (top), the solar wind mass flux at 1AU, $(\rho v_r)_{0.1\text{AU}}(\text{g cm}^{-2} \text{ s}^{-1})$ (middle), and solar wind speed at 1AU, $v_{r,0.1\text{AU}}(\text{km s}^{-1})$, (bottom) as functions of $\langle dv_{\perp,0} \rangle(\text{km s}^{-1})$. On the right axis of the middle panel, we show the proton flux at 1AU, $(n_p v_r)_{1\text{AU}}[\text{cm}^{-2} \text{ s}^{-1}]$. When deriving $(n_p v_r)_{1\text{AU}}$ from $(\rho v_r)_{0.1\text{AU}}$, we use the relation of $\rho v_r \propto r^{-2}$, and assume that mean molecular weight equals to 0.6. T_{max} and $(\rho v_r)_{0.1\text{AU}}$ have positive correlation with $\langle dv_{\perp,0} \rangle$. The dependence of $(\rho v_r)_{0.1\text{AU}}$ is quite steep because of the nonlinearity of the Alfvén waves as explained above. On the other hand, the dependence of T_{max} is more gradual due to the redistribution of the temperature by the thermal conduction. On the other hand, $v_{r,0.1\text{AU}}$ has negative correlation with $\langle dv_{\perp,0} \rangle$ for $\langle dv_{\perp,0} \rangle \geq 0.4(\text{km s}^{-1})$. This is because in lower $\langle dv_{\perp,0} \rangle$ cases the acceleration of less dense plasma is so effective. For $\langle dv_{\perp} \rangle = 0.3(\text{km s}^{-1})$, the coronal temperature and the mass flux of solar wind be-

comes smaller later epoch and the wind speed varies quite a lot; we use the upper limits for T_{max} and $(\rho v_r)_{0.1\text{AU}}$, and dashed error bars for $v_{r,0.1\text{AU}}$.

In our simulation we only consider the steady fluctuations with constant $\langle dv_{\perp,0} \rangle$ to study the basic relation between the footprint fluctuations and the properties of the solar winds. In the real situation, however, $\langle dv_{\perp,0} \rangle$ would vary in time. Our results imply that a tiny temporal variation of $\langle dv_{\perp,0} \rangle$ at the surface possibly leads to large time dependent behaviors of the solar winds. As one example we would like to discuss an event of the solar wind disappearance in the following section.

4.1.4. Disappearance of Solar Wind

On May 10-12, 1999, observed solar wind density near the earth drastically decreases well below 1 cm^{-3} for \sim a day and to 0.1 cm^{-3} at the lowest level, in comparison with the typical value $\sim 5 \text{ cm}^{-3}$ [Le et al., 2000; Smith et al., 2001]. Various mechanisms are widely discussed to explain this disappearance event [Usmanov et al., 2000; Richardson et al., 2000; Crooker et al., 2000]. In §4.1.3, we have shown that the solar wind density sensitively depends on the amplitude of the photospheric fluctuations provided that the nonlinear dissipation of the low-frequency Alfvén waves operates in the solar wind heating and acceleration. According to Figure 11 the solar wind density and mass flux becomes ~ 100 and ~ 50 times smaller respectively if $\langle dv_{\perp,0} \rangle$ changes from 0.7 km/s to 0.4 km/s ; small variance of the energy injection at the solar surface leads to large variation of the solar wind density because of the nonlinearity. Therefore, we can infer that if the amplitude of the photospheric turbulences becomes \sim half during \sim a day, this events of the solar wind disappearance is possibly realized.

The observation shows that velocity of the sparse plasma discussed above is lower than the surrounding value, which is inconsistent with our results (§4.1.3). The stream interaction would resolve the inconsistency. The sparse region is easily blocked by the preceding dense plasma in the spiral magnetic fields (Parker spiral) even if its speed in the inner region (say $\sim 0.1 \text{ AU}$) is faster [Usmanov et al., 2000], because the ram pressure is much smaller than that of the surrounding plasma. For quantitative arguments, however, two dimensional modeling is required.

4.2. Flux Tube properties

It is widely known that the field strength and geometry of the open flux tubes are important parameters to control the solar wind speed. Wang & Sheeley [1990, 1991] showed that the solar wind speed at $\sim 1 \text{ AU}$ is anticorrelated with f_{max} from their long-term observations as well as by a simple theoretical model. Fisk et al. [1999] claimed that the wind speed should be positively correlated with $B_{r,0}$ by simple energetics consideration. Kojima et al. [2005] and Hakamada et al. [2005] have found that the solar wind velocity is better correlated with the combination of these two parameters, $B_{r,0}/f_{\text{max}}$, than $1/f_{\text{max}}$ or $B_{r,0}$ from the comparison of the outflow speed obtained by their interplanetary scintillation measurements with observed photospheric

field strength. Suzuki [2004] and Suzuki et al. [2005b] also pointed out that $B_{r,0}/f_{\max}$ should be the best control parameter provided that the Alfvén waves play a dominate role in the coronal heating and solar wind acceleration.

Here we test the last scenario by our simulation. In Figures 12 and 13, we compare the results of the flux tube with smaller $B_{r,0}/f_{\max} = 322(\text{G})/450$ (Run VIII) with the fiducial case ($B_{r,0}/f_{\max} = 161(\text{G})/75$) (Run II) for the polar coronal holes. We chose the parameters of Run VIII with equatorial and mid-latitude coronal holes in mind; they are surrounded by closed structures, and thus, have moderately larger photospheric field strength and much larger flux tube divergence than the polar coronal holes.

Figure 12 shows that Run VIII gives much slower solar wind speed which is consistent with Kojima et al. [2005], Suzuki [2004], and [Suzuki et al., 2005b], with slightly hotter and denser corona. These results can be understood by the positions of the wave dissipation. The upper panel of Figure 13 indicates that the outgoing Alfvén waves dissipate more rapidly in the smaller $B_{r,0}/f_{\max}$ case. This is because the nonlinearity of the Alfvén waves, $\langle \delta v_{A,+}/v_A \rangle$ is larger due to smaller $v_A \propto B_r$ ($\propto B_{r,0}/f_{\max}$ in the outer region where the flux tube is already super-radially open) even though the absolute amplitude (δv_{\perp}) is smaller (bottom panel of Figure 12). As a result, more wave energy dissipate in the smaller $B_{r,0}/f_{\max}$ case in the subsonic region and less energy remains in the supersonic region. In general, energy and momentum inputs in the supersonic region gives higher wind speed, while those in the subsonic region raises the mass flux (ρv_r) of the wind by an increase of the density [Lamers & Cassinelli, 1999]. Therefore, the smaller $B_{r,0}/f_{\max}$ case gives slower wind with higher coronal density, whereas the solar wind density in the outer region is similar to that of the larger $B_{r,0}/f_{\max}$ case on account of the dilution of the plasma in more rapidly expanding flux tube. We can conclude that $B_{r,0}/f_{\max}$ controls the solar wind speed and the coronal density through the nonlinear dissipation of the Alfvén waves.

4.3. Summary of Parameter Studies

We have examined dependences of the coronal and wind properties on various wave and flux tube parameters in §4.1 and §4.2. One of the important results is that we do not find any subsonic ‘breeze’ solution in our simulations. All the Runs show the transonic feature, hence, the transonic solar winds are natural consequence of the dissipation of the low-frequency Alfvén waves. Smaller energy injection only reduces the density (and consequently the mass flux) of the wind. The wind speed itself is rather faster for smaller wave energy owing to the low density.

From §4.1.1 and §4.1.2, we can conclude that the dependences on the spectra and polarizations of the input fluctuations are weak as long as the low-frequency ($\lesssim 0.05\text{Hz}$) waves are considered. $\langle dv_{\perp,0} \rangle$ and $B_{r,0}/f_{\max}$ are the important control parameters, and the dependences are summarized below:

- The coronal temperature and the density in the corona and solar wind are mainly determined by the photospheric amplitude, $\langle dv_{\perp,0} \rangle$. The corona with temperature $\gtrsim 10^6\text{K}$ is formed if $\langle dv_{\perp,0} \rangle \gtrsim 0.7\text{km s}^{-1}$. Larger $\langle dv_{\perp,0} \rangle$ gives higher density in the corona and the solar wind. If $\langle dv_{\perp,0} \rangle \lesssim 0.3\text{km s}^{-1}$ the hot plasma cannot be maintained and the mass flux of the solar wind is unrealistically small.
- The solar wind speed is mainly controlled by $B_{r,0}/f_{\max}$; faster winds come from open flux tubes with larger $B_{r,0}/f_{\max}$.

5. Fast and Slow Solar Winds

The observed solar winds can be categorized into two distinctive types. One is the fast solar wind which is mainly from the polar coronal holes and the other is the slow wind which is from the mid- to low-latitude regions. Apart from the velocity difference, both the density of the solar winds [Phillips et al., 1995] and the freezing-in temperature of the heavy ions [Geiss et al., 1995] which reflects the coronal temperature are anticorrelated with the velocity. Origins of the slow solar winds are still in debate; there are mainly two types argued (see Wang et al.2000 for review). One is the acceleration due to the intermittent break-up of the cusp-shaped closed fields in the equatorial region (e.g. Endeve, Leer, & Holtzer 2003). The other is the acceleration in the open flux tube with large areal expansion in the low- and mid-latitude corona. Kojima et al. [1999] detected low-speed winds with a single magnetic polarity, originating from open structure regions located near an active region, which indicates a certain fraction of the slow streams is coming from the open regions, similarly to the fast winds. In this paper we focus on the latter case with respect to the slow solar winds.

Based on our simulation results, the coronal and solar wind density is mainly controlled by the input wave amplitude, while the solar wind speed is determined by the field strength and the geometry of the flux tubes. Referring these, we can infer the suitable $\langle dv_{\perp,0} \rangle$ and $B_{r,0}/f_{\max}$ for the slow solar wind by comparing with those for the fast wind (Run I/II; also in paper I); the slow wind requires larger $\langle dv_{\perp,0} \rangle$ and smaller $B_{r,0}/f_{\max}$ than the fast wind. The adopted parameters are summarized in table 1 (Run X).

In the panels on the left side of Figure 14 we compare the results of Run X (slow wind) and Run I (fast wind) overlaid with the recent observations of slow solar winds (see Figure 2 for the observations of the fast winds). The temperature and density of the slow wind case becomes larger on account of the larger $\langle dv_{\perp,0} \rangle$, which explains the observations. On the other hand, smaller $B_{r,0}/f_{\max}$ gives slower terminal speed. As a result, the observed anticorrelation of the wind speed and the coronal temperature [Schwadron & McComas, 2003] is well-explained by our simulations. In the slow wind case (Run X), the acceleration of the outflow is more gradual, and it is not negligible in $r \gtrsim 20r_{\odot}$ (e.g. Nakagawa et al.2005).

In the panels on the right of Figure 14, we show the properties of the wave dissipation. The top right panel compares

transverse amplitude, $\langle dv_{\perp} \rangle$, averaged over 30 minutes in the fast and slow wind cases. $\langle dv_{\perp} \rangle$ is larger in the fast wind. This is because the Alfvén waves become less dissipative in the fast wind conditions; larger $B(\propto B_0/f_{\max})$ and smaller ρ gives larger v_A so that the nonlinearity of the Alfvén waves, $\delta v_{A,+}/v_A$, is systematically smaller. As a result, the Alfvén wave dissipates more slowly in the fast wind case, which is shown in the plot of S_c of the wave (the bottom right panel of Figure 14). This tendency of the larger $\langle dv_{\perp} \rangle$ in the fast wind is expected to continue to the outer region, $\gtrsim 1\text{AU}$. Various in situ observations in the solar wind plasma near the earth also show that the fast streams contain more Alfvénic wave components (see Tsurutani & Ho 1999 for review), which can be explained via the nonlinear dissipation of the Alfvén waves based on our simulation.

The middle right panel of Figure 14 shows longitudinal fluctuation, $\langle dv_{\parallel} \rangle$, averaged over 30 minutes. $\langle dv_{\parallel} \rangle$ reflects the amplitude of the slow MHD waves generated from the Alfvén waves via the nonlinear process (§3). Slow waves are identified in polar regions [Ofman et al., 1999] and low-latitude regions [Sakurai et al., 2002] at low altitude ($r \lesssim 1.2R_{\odot}$). The observed amplitudes are still small ($\simeq 7.5\text{km s}^{-1}$ in the polar regions and $\simeq 0.3\text{km s}^{-1}$ in the low-latitude regions) because of the large density there, which is consistent with our results. What is more interesting is the longitudinal fluctuations in outer regions. Our results exhibit that $\langle dv_{\parallel} \rangle$ in the solar wind plasma is not small. Typically, the simulations give $\langle dv_{\parallel} \rangle \sim 100\text{km/s}$ in $3R_{\odot} \lesssim r \lesssim 10R_{\odot}$ of the fast wind and $\langle dv_{\parallel} \rangle \sim 20\text{km/s}$ in $2R_{\odot} \lesssim r \lesssim 10R_{\odot}$ of the slow wind, whereas these might be modified if we take into account multi-dimensional effects (§6.2). This is directly testable by in situ measurements of future missions, Solar Orbiter and Solar Probe, which will approach to ~ 45 and $4R_{\odot}$, respectively, corresponding to the inside of our computation domain.

Our simulations show that the different types of the solar winds can be explained by the single process, the dissipation of the low-frequency Alfvén waves, although we do not intend to exclude other possibilities. The varieties of the solar winds are due to the varieties of the footpoint amplitude as well as the magnetic field and geometry of the flux tubes. Our choice of $B_{r,0}/f_{\max}$ is consistent with the obtained data by Kojima et al. [2005] and Hakamada et al. [2005] who report that the slow winds are mainly from the low-to mid-latitude coronal holes with smaller $B_{r,0}/f_{\max}$. In contrast, quantitative arguments on $\langle dv_{\perp,0} \rangle$ need more fine scale observations of the magnetic fields with high cadence by future telescopes such as Solar-B.

6. Discussions

6.1. Wave Generation

In this paper we have assumed that the origin of the waves is the steady turbulent motions at the photosphere. However, transient activities are also expected to play a role in the wave generation. Sturrock [1999] proposed small flare-like events triggered by magnetic reconnections of closed

loops in the chromosphere excite MHD waves in the corona. Miyagoshi et al. [2005] also show that interactions between open field lines and emergent flux tubes excite Alfvén waves at location above the photosphere. These waves could directly heat up the corona since they do not suffer the attenuation in the chromosphere and the TR.

An important issue for the wave generation by these transient events is the energetics. The energy release from each event is generally thought to be small, categorized as micro- or nano-flares [Parnell & Jupp, 2000; Katsukawa & Tsuneta, 2001]. To clarify how these waves dominantly work in the heating and acceleration of the solar wind, we should determine the frequency of these events. These small-scale events might be important in the heating not only of the open coronal holes but of the closed regions. The determination of the total energy release from the small transient events by future observations is quite important in terms of the coronal heating in various portions of the corona.

6.2. Limitation of Our Simulations

We have shown by the self-consistent simulation that the dissipation of the low-frequency Alfvén waves through the generation of the compressive waves and shocks is one of the solutions for the heating and acceleration of the plasma in the coronal holes. However, the validity of the 1D MHD approximation we are adopting needs to be examined.

First of all, we think that the MHD approximation is still appropriate for the studies of the average properties of the plasma. This is because the Larmor radii of the ions due to the fluctuation of the field lines, B_{\perp} , are smaller than the shortest wavelength considered (waves with a period 20s) in the entire regions. Therefore, the particles of each component can be sufficiently randomized.

However, effects of multi-component plasma need to be taken into account [Lie-Svendsen, 2001]. The thermal conduction and radiative cooling are involved with the electrons, and the electron temperature becomes systematically lower than the ion temperature without effective thermal coupling by Coulomb collisions. The observed proton temperature is actually higher than the electron temperature even around a few solar radii [Esser et al., 1999]. The temperature in our simulations represents the electron temperature. The actual thermal pressure is supposed to be higher than the simulated temperature due to the higher proton temperature, so that the acceleration profile might be slightly modified.

Collisionless processes would also be important for the wave dissipation [Tsurutani et al., 2005]. The heating rate by the dissipation of the Alfvén waves is different for electrons and ions [Tsiklauri et al., 2005]. The compressive waves generated from the Alfvén waves suffer transit time damping by interactions between the magnetic mirrors and the surfing particles [Barnes, 1966; Suzuki et al., 2005a]. If the high-frequency (ioncyclotron) waves exist by the frequency cascade, the heating sensitively depends on mass-to-charge ratio of the particles [Dusenbery & Hollweg, 1981; Marsch et al., 1982]. It is believed that this process is promising to explain the observed preferential heating of the perpendicular temperature of the heavy ions [Kohl et al., 1998].

In the chromosphere, the gas is not fully ionized. In such circumstances, the friction due to the ion-neutral collisions might be important in the dissipation of Alfvén waves [Lazarian et al., 2004; Yan & Lazarian, 2004].

Generally, the shock dissipation tends to be overestimated in 1D simulations because the shocks cannot be diluted by the geometrical expansion. On the other hand, there are other mechanisms of the wave damping due to the multi-dimensionality [Ofman, 2004], such as phase mixing [Heyvaerts & Priest, 1983; Nakariakov et al., 1998; De Moortel et al., 2000] and refraction [Bogdan et al., 2003]. Moreover, the solar wind plasma is more or less turbulent and it must be important to take into account the plasma heating through the cascade of Alfvénic turbulences in the transverse direction [Goldreich & Sridhar, 1995; Mattheus et al., 1999; Oughton et al., 2001]. Studies of the imbalanced cascade, in which wave component in one direction has larger energy than that in the counter direction, is particularly essential to understand the transport phenomena in the solar wind plasma [Lithwick & Goldreich, 2003], though it has not been fully understood at the moment.

Therefore, the Alfvén waves might also be dissipated by paths different from those discussed in this paper. Accordingly, $\langle dv_{\parallel} \rangle$ might be modified when these multi-dimensional dissipation processes are considered. Self-consistent simulations including these various processes remain to be done to give the final conclusion.

7. Summary

We have studied the universality and diversity of the coronal heating and solar wind acceleration by the low-frequency Alfvén waves in the open coronal holes. We have performed 1D MHD numerical simulation from the photosphere to 0.3 or 0.1AU. The low-frequency Alfvén waves with various spectra, polarization, and amplitude are generated by the footpoint fluctuations of the magnetic field lines. We have treated the wave propagation and dissipation, and the heating and acceleration of the plasma in a self-consistent manner.

We have found that the transonic solar winds are accomplished in all the simulation Runs. Smaller energy injection does not reduce the outflow speed but the density to maintain the transonic feature. The atmosphere is heated up to the coronal temperature ($\gtrsim 10^6\text{K}$) if the photospheric amplitude, $\langle dv_{\perp,0} \rangle \gtrsim 0.7\text{km s}^{-1}$. Otherwise, the temperature and density become much lower than the present coronal values. If $\langle dv_{\perp,0} \rangle \lesssim 0.3\text{km s}^{-1}$, the temperature becomes less than a few 10^5K and the sufficient mass cannot be supplied into the corona owing to the suppression of the chromospheric evaporation. The stable hot corona cannot be maintained any longer, and the mass flux of the solar wind becomes at least 3 orders of magnitude smaller than the observed value of the present solar wind. This shows that the solar wind almost disappears only by reducing the photospheric fluctuation amplitude by half. On the other hand, the case with $\langle dv_{\perp,0} \rangle = 1.4\text{km s}^{-1}$ gives 10 times larger density than the fiducial case ($\langle dv_{\perp,0} \rangle = 0.7\text{km s}^{-1}$). These sensi-

tive behaviors of the solar wind mass flux on $\langle dv_{\perp,0} \rangle$ can be explained via the nonlinear dissipation of the Alfvén waves. Our simulations have also confirmed that the positive correlation of the solar wind speed with $B_{r,0}/f_{\text{max}}$ obtained by Kojima et al. [2005] and Hakamada et al. [2005].

We have finally pointed out that both fast and slow solar winds can be explained even solely by the dissipation of the low-frequency Alfvén waves with different $\langle dv_{\perp,0} \rangle$ and $B_{r,0}/f_{\text{max}}$, whereas we do not intend to exclude other possibilities. The fast winds are from flux tubes with larger $B_{r,0}/f_{\text{max}}$ and smaller $\langle dv_{\perp,0} \rangle$, while the slow winds are from flux tubes with smaller $B_{r,0}/f_{\text{max}}$ and larger $\langle dv_{\perp,0} \rangle$. These choices naturally explain the following observed tendencies: (i) the anticorrelation of the solar wind speed and the coronal temperature, and (ii) the larger amplitude of Alfvén waves in the fast winds in the interplanetary space. The tendency with respect to $B_{r,0}/f_{\text{max}}$ is consistent with the observed trend [Kojima et al., 2005]. To determine $\langle dv_{\perp,0} \rangle$ in various coronal holes, fine scale observations of the magnetic fields with high cadence are required; this is one of the suitable targets for Solar-B which is to be launched in 2006.

Acknowledgments. We thank Profs. Kazunari Shibata, Alex Lazarian, and Bruce Tsurutani for many fruitful discussions. This work is in part supported by a Grant-in-Aid for the 21st Century COE ‘‘Center for Diversity and Universality in Physics’’ from the Ministry of Education, Culture, Sports, Science, and Technology (MEXT) of Japan. T.K.S. is financially supported by the JSPS Research Fellowship for Young Scientists, grant 4607. SI is supported by the Grant-in-Aid (15740118, 16077202) from the MEXT of Japan.

Appendix A: Outgoing Boundary Condition

We introduce our prescription for the outgoing boundary condition of the MHD waves. The method is similar to that in Wu et al. [2001], while ours is implemented for stable treatment of strong MHD shocks.

Basic MHD equations can be expressed in a matrix form as

$$\frac{\partial \mathbf{U}}{\partial t} + \mathbf{A} \frac{\partial \mathbf{U}}{\partial r} + \mathbf{C} = 0. \quad (\text{A1})$$

\mathbf{U} and \mathbf{A} are explicitly written as

$$\mathbf{U} = \begin{pmatrix} v_r \\ v_{\perp,1} \\ v_{\perp,2} \\ B_{\perp,1} \\ B_{\perp,2} \\ \rho \\ s \end{pmatrix},$$

$$\mathbf{A} = \begin{pmatrix} v_r & 0 & 0 & \frac{B_{\perp,1}}{4\pi\rho} & \frac{B_{\perp,2}}{4\pi\rho} & c_s^2/\rho & p/s\rho \\ 0 & v_r & 0 & -\frac{B_r}{4\pi\rho} & 0 & 0 & 0 \\ 0 & 0 & v_r & 0 & -\frac{B_r}{4\pi\rho} & 0 & 0 \\ B_{\perp,1} & -B_r & 0 & v_r & 0 & 0 & 0 \\ B_{\perp,2} & 0 & -B_r & 0 & v_r & 0 & 0 \\ \rho & 0 & 0 & 0 & 0 & v_r & 0 \\ 0 & 0 & 0 & 0 & 0 & 0 & v_r \end{pmatrix},$$

where $s \equiv p/\rho^\gamma$ and $c_s = \sqrt{\gamma p/\rho}$, and subscripts, $\perp, 1$ and $\perp, 2$, denote first and second transverse components. \mathbf{C}

consists of terms due to external force, additional heating and cooling, and curvature. In our case, we have taken into account gravity, thermal conduction, radiative cooling, and superradial expansion of flux tubes:

$$\mathbf{C} = \begin{pmatrix} F_1 \left(\frac{B_{\perp,1}^2}{4\pi\rho} - v_{\perp}^2 \right) + \frac{GM_{\odot}}{r^2} \\ F_1 (v_r v_{\perp,1} - \frac{B_r B_{\perp,1}}{4\pi\rho}) \\ F_1 (v_r v_{\perp,2} - \frac{B_r B_{\perp,2}}{4\pi\rho}) \\ F_1 (B_{\perp,1} v_r - B_r v_{\perp,1}) \\ F_1 (B_{\perp,2} v_r - B_r v_{\perp,2}) \\ F_2 \rho v_r \\ \frac{\rho^{1-\gamma}}{\gamma-1} \left(\frac{1}{\rho r^2 f} \frac{\partial}{\partial r} (r^2 f F_c) + \frac{q_B}{\rho} \right) \end{pmatrix},$$

where $F_1 \equiv \frac{1}{r\sqrt{f}} \frac{\partial}{\partial r} (r\sqrt{f})$ and $F_2 \equiv \frac{1}{r^2 f} \frac{\partial}{\partial r} (r^2 f)$ are arising from the geometrical effect, and $B_{\perp}^2 \equiv B_{\perp,1}^2 + B_{\perp,2}^2$ and $v_{\perp}^2 \equiv v_{\perp,1}^2 + v_{\perp,2}^2$. Please note that \mathbf{C} is negligible except for the thermal conduction term ($\frac{1}{\rho r^2 f} \frac{\partial}{\partial r} (r^2 f F_c)$) in our simulations if r_{out} is set at a sufficiently distant location.

Using eigen values, λ_i ($i = 1, \dots, 7$), and eigen vectors, \mathbf{I}_i , defined as

$$\mathbf{I}_i A = \lambda_i \mathbf{I}_i, \quad (\text{A2})$$

we can derive characteristic equations for the seven MHD waves from eq.(A1) :

$$\mathbf{I}_i \frac{\partial \mathbf{U}}{\partial t} + \lambda_i \mathbf{I}_i \frac{\partial \mathbf{U}}{\partial r} + \mathbf{I}_i \cdot \mathbf{C} = 0 \quad (\text{A3})$$

λ_i corresponds to phase speeds of the respective waves,

$$\lambda_1 = v_r + v_f, \quad \lambda_2 = v_r + v_A, \quad \lambda_3 = v_r + v_s, \quad \lambda_4 = v_r,$$

$$\lambda_5 = v_r - v_s, \quad \lambda_6 = v_r - v_A, \quad \lambda_7 = v_r - v_f, \quad (\text{A4})$$

where $v_f = \sqrt{\frac{1}{2} [c_s^2 + \frac{B^2}{4\pi\rho} + \sqrt{(c_s^2 + \frac{B^2}{4\pi\rho})^2 - 4 \frac{c_s^2 B_{\perp}^2}{4\pi\rho}]}$, $v_A = \frac{B_r}{\sqrt{4\pi\rho}}$, and

$v_s = \sqrt{\frac{1}{2} [c_s^2 + \frac{B^2}{4\pi\rho} - \sqrt{(c_s^2 + \frac{B^2}{4\pi\rho})^2 - 4 \frac{c_s^2 B_{\perp}^2}{4\pi\rho}]}$ are phase speeds of fast, Alfvén, and slow modes, respectively. Here we define total magnetic field by $B^2 = B_r^2 + B_{\perp}^2$. The eigen vectors are explicitly written as

$$\mathbf{I}_1 = (\rho v_f (v_f^2 - v_A^2), -\frac{B_r B_{\perp,1}}{4\pi} v_f, -\frac{B_r B_{\perp,2}}{4\pi} v_f,$$

$$\frac{B_{\perp,1}^2}{4\pi} v_f^2, \frac{B_{\perp,2}^2}{4\pi} v_f^2, c_s^2 (v_f^2 - v_A^2), p/s (v_f^2 - v_A^2))$$

$$\mathbf{I}_2 = (0, B_{\perp,2}, -B_{\perp,1}, -\frac{B_{\perp,2}}{\sqrt{4\pi\rho}}, \frac{B_{\perp,1}}{\sqrt{4\pi\rho}}, 0, 0)$$

$$\mathbf{I}_3 = (\rho v_s (v_s^2 - v_A^2), -\frac{B_r B_{\perp,1}}{4\pi} v_s, -\frac{B_r B_{\perp,2}}{4\pi} v_s,$$

$$\frac{B_{\perp,1}^2}{4\pi} v_s^2, \frac{B_{\perp,2}^2}{4\pi} v_s^2, c_s^2 (v_s^2 - v_A^2), p/s (v_s^2 - v_A^2))$$

$$\mathbf{I}_4 = (0, 0, 0, 0, 0, 0, 1)$$

$$\mathbf{I}_5 = (\rho v_s (v_s^2 - v_A^2), -\frac{B_r B_{\perp,1}}{4\pi} v_s, -\frac{B_r B_{\perp,2}}{4\pi} v_s,$$

$$-\frac{B_{\perp,1}^2}{4\pi} v_s^2, -\frac{B_{\perp,2}^2}{4\pi} v_s^2, -c_s^2 (v_s^2 - v_A^2), -p/s (v_s^2 - v_A^2))$$

$$\mathbf{I}_6 = (0, B_{\perp,2}, -B_{\perp,1}, \frac{B_{\perp,2}}{\sqrt{4\pi\rho}}, -\frac{B_{\perp,1}}{\sqrt{4\pi\rho}}, 0, 0)$$

$$\mathbf{I}_7 = (\rho v_f (v_f^2 - v_A^2), -\frac{B_r B_{\perp,1}}{4\pi} v_f, -\frac{B_r B_{\perp,2}}{4\pi} v_f,$$

$$-\frac{B_{\perp,1}^2}{4\pi} v_f^2, -\frac{B_{\perp,2}^2}{4\pi} v_f^2, -c_s^2 (v_f^2 - v_A^2), -p/s (v_f^2 - v_A^2))$$

The characteristic equations enable us to implement the outgoing boundary condition in a clear and direct manner. All the incoming waves should be removed for the proper outgoing boundary. This is accomplished by setting physical variables, \mathbf{U} , to be a constant in space for the incoming characteristics [Thompson, 1987]. Then, we simply impose following condition at $r = r_{\text{out}}$:

$$\left(\mathbf{I}_i \frac{\partial \mathbf{U}}{\partial t} + \mathcal{L}_i + \mathbf{I}_i \cdot \mathbf{C} \right) \Big|_{r_{\text{out}}} = 0, \quad (\text{A5})$$

where

$$\mathcal{L}_i = \begin{cases} \lambda_i \mathbf{I}_i \frac{\partial \mathbf{U}}{\partial r} & : \lambda_i > 0 \text{ (Outgoing)} \\ 0 & : \lambda_i < 0 \text{ (Incoming)} \end{cases} \quad (\text{A6})$$

In our scheme, we firstly perform time evolution to derive \mathbf{U}_j^n ($1 \leq j < j_{\text{out}}$) at time n except the outermost grid, j_{out} , from \mathbf{U}_j^{n-1} ($1 \leq j \leq j_{\text{out}}$) at previous time step, $n-1$, by the second order MHD Godunov-MOCCT scheme. The physical variables at the outermost grid, $\mathbf{U}_{j_{\text{out}}}^n$ are determined at the end of each time step by using $\mathbf{U}_{j_{\text{out}}}^{n-1}$ and $\mathbf{U}_{j_{\text{out}-1}}^n$. At this time we integrate eq.(A5) implicitly in time for numerical stability:

$$(\mathbf{I}_i)_{j_{\text{out}}}^n \frac{\mathbf{U}_{j_{\text{out}}}^n - \mathbf{U}_{j_{\text{out}}}^{n-1}}{\Delta t} + (\mathcal{L}_i)_{j_{\text{out}}}^n + (\mathbf{I}_i \cdot \mathbf{C})_{j_{\text{out}}}^n = 0. \quad (\text{A7})$$

We adopt upwind discretization for spatial derivative appeared in \mathcal{L}_i for the outgoing characteristic, ($\frac{\partial \mathbf{U}}{\partial r} \Big|_{j_{\text{out}}}^n = \frac{\mathbf{U}_{j_{\text{out}}}^n - \mathbf{U}_{j_{\text{out}-1}}^n}{\Delta r}$). Note that $(\mathbf{I}_i)_{j_{\text{out}}}^n$, $(\mathcal{L}_i)_{j_{\text{out}}}^n$, and $\mathbf{C}_{j_{\text{out}}}^n$ are functions of $\mathbf{U}_{j_{\text{out}}}^n$, so we need iteration to determine $\mathbf{U}_{j_{\text{out}}}^n$. Equation (A7) determines the physical quantities at the outermost mesh to satisfy the outgoing condition for all the seven MHD characteristics.

We carry out reflection tests for our implementation by using different types of waves with various amplitudes from linear to extremely nonlinear regimes. We here consider two types of waves as typical examples : (i) Alfvén waves, and (ii) oblique fast waves which propagate in 45 degree with respect to the underlying magnetic field. We use Cartesian coordinate with the homogeneous background for the tests. Solitary waves which travel in the right direction are initially set, and the outgoing condition is implemented at the right boundary. In order to give the waves which purely propagate in one direction even in the extremely nonlinear regime, we adopt the simple wave solutions. For Alfvén waves, the circularly polarized Alfvén waves traveling in one direction are the exact solutions of the basic MHD equations. For the

oblique fast waves, ρ , p , v_x , and v_y can be expressed by B_y [Wu, 1987]:

$$\frac{d\rho}{dB_y} = \frac{B_y}{4\pi} \frac{1}{v_f^2 - c_s^2}, \quad (\text{A8})$$

$$\frac{dv_x}{dr} = \frac{B_y}{4\pi\rho} \frac{v_f}{v_f^2 - c_s^2}, \quad (\text{A9})$$

$$\frac{dv_y}{dB_y} = -\frac{B_x}{4\pi\rho v_f}, \quad (\text{A10})$$

$$\frac{dp}{dB_y} = \frac{B_y}{4\pi} \frac{c_s^2}{v_f^2 - c_s^2}. \quad (\text{A11})$$

Note that we can treat the fast (and slow) waves in two dimensional (x & y) space without loss of generality because they are coplanar, while the three dimensional space is required for the circularly polarized Alfvén waves. We initially give sinusoidal variation of B_y for the fast waves and the other quantities are determined by eqs.(A8) - (A11). If the wave amplitude, δv , is sufficiently smaller than v_f , all the quantities can be approximated by sinusoidal variations.

Figure 15 shows an example of the reflection tests for the oblique fast waves. We non-dimensionalize the B values by $1/4\pi \rightarrow 1$. The initial background conditions are, $\rho = 1$, $p = 1$, $B_x = 1.5$, $B_y = 1.5$, $v_x = 0$, and $v_y = 0$, which give plasma β value, $\beta = 2p/B^2 (= 8\pi p/B^2$ in Gauss-cgs unit) = 0.44. We give magnetic field amplitude, $\delta B_y = 6.5$, which corresponds to relatively strong non-linearity, $\delta v/v_f = 3.1$. The simulation box is from $x = 0$ to $x = 4$ and the number of grid points is 512. The initial solitary wave is put between $x = 2$ and 3. The initial condition ($t = 0$) and results at $t = 0.6$ are plotted in dashed and solid lines. To estimate errors at the right boundary, we also carry out simulation in larger box between $x = 0$ and 8(dotted lines), which is free from the boundary errors at $x = 4$.

Because of the strong nonlinearity, the wave rapidly steepen to form shocks before reaching $x = 4$. These shocks travel to the right direction, which are seen in the simulation with the larger box size (dotted lines). At $t = 0.6$, the main part of the wave goes out of the simulation box ($x = 4$) except the trailing edge. The differences between solid and dotted lines indicate errors due to our implementation of the outflow boundary condition. Figure 15 shows the errors are quite small; relative errors to the initial amplitude are at most 1% for each variable. Our implementation is good enough for the passage of the moderately strong shocks.

Figure 16 shows relative errors to the initial amplitude, $\delta v_{\text{error}}/\delta v$ on the normalized wave amplitude, $\delta v/v_f$ and $\delta v/v_A$, for the oblique fast waves and circularly polarized Alfvén waves. As for the relative errors, we plot the errors of v_y , whereas the other quantities (ρ, p, B_y, v_x) give similar results. If $\delta v/v_{\text{ph}} \lesssim 3$ ($v_{\text{ph}} = v_f$ or v_A is phase speed), the relative errors are smaller than 0.01 and our implementation is sufficiently acceptable. The Alfvén wave with $\delta v/v_A = 10$ gives larger $\delta v_{\text{error}}/\delta v \simeq 0.05$. This is because as the wave travels it does not only consist of Alfvén modes but contains non-linear fast and slow wave

components. However, this value ($\delta v_{\text{error}}/\delta v \simeq 0.05$) is still acceptable since an error in energy ($\propto \delta v^2$) is only 0.3%.

Notes

1. It is instructive to note that the incoming Alfvén waves have the positive correlation between v_{\perp} and B_{\perp} (dark-dark or light-light in the figures), while the outgoing modes have the negative correlation (dark-light or light-dark).
2. The phase correlation of the longitudinal slow waves is opposite to that of the transverse Alfvén waves. The outgoing slow modes have the positive correlation between amplitudes of v_r and ρ , ($\delta v_r \delta \rho > 0$), while the incoming modes have the negative correlation ($\delta v_r \delta \rho < 0$).

References

- Anderson, C. S. & Athay, R. G. (1989), Chromospheric and coronal heating, *Astrophys. J.*, , 336, 1089 - 1091
- Aschwanden, M. J., Poland, A. I., & Robin, D. M. (2001), New solar corona ARA&A, 39, 175 - 210
- Axford, W. I. & McKenzie, J. F. (1997), The Solar Wind in "Cosmic Winds and the Heliosphere", Eds. Jokipii, J. R., Sonnet, C. P., and Giampapa, M. S., University of Arizona Press, 31 - 66
- Banerjee, D., Teriaca, L., Doyle, J. G., & Wilhelm, K. (1998), Broadening of SI VIII lines observed in the solar polar coronal holes, *Astron. Astrophys.*, , 339, 208 - 214
- Barnes, A. (1966), Collisionless damping of hydromagnetic waves, *Phys. Fluid*, 9, 1483
- Bogdan, T. J. et al. (2003), Waves in the magnetized solar atmosphere. II. waves from localized sources in magnetic flux concentrations, *Astrophys. J.*, , 500, 626 - 660
- Braginskii, S. I. (1965), *Rev. Plasma Phys.*, 1., 205 - 311
- Canals, A., Breen, A. R., Ofman, L., Moran, P. J., & Fallows, R. A. (2002), Estimating random transverse velocities in the fast solar wind from EISCAT interplanetary scintillation measurements, *Ann. Geophys.*, 20, 1265 - 1277
- Cho, J. & Lazarian, A. (2002), Compressible Sub-Alfvénic MHD Turbulence in Low- β Plasmas, *Phys. Rev. Lett.*, , 88, 245001
- Cho, J. & Lazarian, A. (2003), Compressible magnetohydrodynamic turbulence: mode coupling, scaling relations, anisotropy, viscosity-damped regime and astrophysical implications, *Mon. Not. R. Astron. Soc.*, , 345, 325 - 339
- Cranmer, S. R. (2000), Ion cyclotron wave dissipation in the solar corona: *Astrophys. J.*, , 532, 1197 - 1208
- Cranmer, S. R. & van Ballegoijen, A. A. (2003), Alfvénic turbulence in the extended solar corona: kinetic effects and proton heating, *Astrophys. J.*, , 594, 573 - 591
- Cranmer, S. R. & van Ballegoijen, A. A. (2005), On the Generation, Propagation, and Reflection of Alfvén Waves from the Solar Photosphere to the Distant Heliosphere, *Astrophys. J. (Supp.)*, , 156, 265 - 293
- Crooker, N. U., Shodhan, S., Cosling, J. T., Simmerer, J., Lepping, R. P., Steinberg, J. T., & Kahler, S. W. (2000), Density extremes in the solar wind, *Geophys. Res. Lett.*, , 27, 3769 - 3772
- De Moortel, I., Hood, A. W., & Arber, T. D. (2000), Phase mixing of Alfvén waves in a stratified and radially diverging, open atmosphere, *Astron. Astrophys.*, , 354, 334 - 348
- Dmitruk, P., Matthaeus, W. H., Milano, L. J., Oughton, S., Zank, G. P., & Mullan, D. J. (2002), Coronal Heating Distribution Due to Low-Frequency, Wave-driven Turbulence, *Astrophys. J.*, , 575, 571 - 577
- Dusenbery, P. B. & Hollweg J. V. (1981), Ion-cyclotron heating and acceleration of solar wind minor ions, *J. Geophys. Res.*, , 86, 153 - 164
- Endeve, E., Leer, E., & Holtzer, T. E. (2003), Two-dimensional Magnetohydrodynamic Models of the Solar Corona: Mass Loss from the Streamer Belt, *Astrophys. J.*, , 589, 1040 - 1053
- Esser, R., Habbal, S. R., Colse, W. A., & Hollweg, J. (1997), Hot protons in the inner corona and their effect on the flow properties of the solar wind, *J. Geophys. Res.*, , 102, 7063 - 7074
- Esser, R., Fineschi, S., Dobrzycka, D., Habbal, S. R., Edgar, R. J., Raymond, J. C., & Kohl, J. L. (1999), Plasma properties in coronal holes derived from measurements of minor ion spectral lines and polarized white light intensity, *Astrophys. J.*, , 510, L63 - L67
- Fisk, L. A., Schwadron, N. A., & Zurbuchen, T. H. (1999), Acceleration of the fast solar wind by the emergence of new magnetic flux, *J. Geophys. Res.*, , 104, A4, 19765 - 19772
- Fludra, A., Del Zanna, G. & Bromage, B. J. I. (1999), EUV observations above polar coronal holes, *Spa. Sci. Rev.*, 87, 185 - 188

- Goldreich, P. & Sridhar, S. (1995), Toward a theory of interstellar turbulence. 2: Strong Alfvénic turbulence, *Astrophys. J.*, , 438, 763 - 775
- Goldstein, M. L. (1978), An instability of finite amplitude circularly polarized Alfvén waves, *Astrophys. J.*, , 219, 700 - 704
- Grall, R. R., Coles, W. A., Klingensmith, M. T., Breen, A. R., Williams, P. J. S., Markkanen, J., & Esser, R. (1996), Rapid acceleration of the polar solar wind, *Nature*, 379, 429 - 432
- Geiss, J. et al. (1995), The southern high-speed stream : results from the SWICS instrument on Ulysses, *science*, 268, 1033 - 1036
- Habbal, S. R., Esser, R., Guhathakura, M., & Fisher, R. R. (1994), Flow properties of the solar wind derived from a two-fluid model with constraints from white light and in situ interplanetary observations, *Geophys. Res. Lett.*, , 22, 1465 - 1468
- Hakamada, K., Kojima, M., Ohmi, T., Tokumaru, M., & Fujiki, K. (2005), Correlation between Expansion Rate of the Coronal Magnetic Field and Solar Wind Speed in a Solar Activity Cycle, *Sol. Phys.*, , 227, 387
- Hayes, A. P., Vourlidas, A., & Howard, R. A. (2001), Deriving the Electron Density of the Solar Corona from the Inversion of Total Brightness Measurements, *Astrophys. J.*, , 548, 1081
- Heyvaerts, J. & Priest, E. R. (1983), Coronal heating by phase-mixed shear Alfvén waves, *Astron. Astrophys.*, , 117, 220 - 234
- Hollweg, J. V. (1982), Heating of the corona and solar wind by switch-on shocks, *Astrophys. J.*, , 254, 806 - 813
- Holweber, H., Gehlsen, M., & Ruland, F. (1978), Spatially-averaged properties of the photospheric velocity field, *Astron. Astrophys.*, , 70, 537 - 542
- Isenberg, P. A. & Hollweg, J. V. (1983), On the preferential acceleration and heating of solar wind heavy ions, *J. Geophys. Res.*, , 88, 3923 - 3935
- Jacques, S. A. (1977), Momentum and energy transport by waves in the solar atmosphere and solar wind, *Astrophys. J.*, , 215, 942 - 951
- Katsukawa, Y. & Tsuneta, S. (2001), Small Fluctuation of Coronal X-Ray Intensity and a Signature of Nanoflares, *Astrophys. J.*, , 557, 343 - 350
- Kohl, J. L. et al. (1998), UVCS/SOHO empirical determinations of anisotropic velocity distributions in the solar corona, *Astrophys. J.*, , 501, L127 - L 131
- Kojima, M., Fujiki, K., Ohmi, T., Tokumaru, M., Yokobe, A., & Hakamada, K. (1999), Low-speed solar wind from the vicinity of solar active regions, *J. Geophys. Res.*, , 104, 16993 - 17004
- Kojima, M., Breen, A. R., Fujiki, K., Hayashi, K., Ohmi, T., & Tokumaru, M. (2004), Fast solar wind after the rapid acceleration, *JGRA*, 109, A04103, 2004
- Kojima, M., K. Fujiki, M. Hirano, M. Tokumaru, T. Ohmi, and K. Hakamada, (2005), "The Sun and the heliosphere as an Integrated System", Giannina Poletto and Steven T. Suess, Eds. Kluwer Academic Publishers, in press
- Kopp, R. A. & Holzer, T. E. (1976), Dynamics of coronal hole regions. I - Steady polytropic flows with multiple critical points, *Sol. Phys.*, 49, 43 - 56
- Kudoh, T. & Shibata, K. (1999), Alfvén wave model of spicules and coronal heating, *Astrophys. J.*, , 514, 493 - 505
- Lamy, P., Quemerais, E., Liebaria, A., Bout, M., Howard, R., Schwenn, R., & Simnett, G. (1997), in Fifth SOHO Workshop, The Corona and Solar Wind near Minimum Activity, ed A. Wilson (ESA-SP 404; Noordwijk:ESA), 491
- Landini, M. & Monsignori-Fossi, B. C. (1990), The X-UV spectrum of thin plasmas, *A&A Supp.*, 82, 229 - 260
- Lamers, H. J. G. L. M. & Cassinelli, J. P. (1999), 'Introduction to Stellar Wind', Cambridge
- Lazarian, A., Vishniac, E. T., & Cho, J. (2004), Magnetic field structure and stochastic reconnection in a partially ionized plasma, *Astrophys. J.*, , 603, 180
- Le, G., Russell, C. T., & Petrinec, S. M. (2000), The magnetosphere on May 11, 1999, the day the solar wind almost disappeared: I. Current systems, *Geophys. Res. Lett.*, , 27, 1827 - 1830
- Lie-Svendsen, Ø, Leer, E., & Hansteen, V. H. (2001), A 16-moment solar wind model: From the chromosphere to 1 AU *J. Geophys. Res.*, , 106, 8217 - 8232
- Lithwick, Y. & Goldreich, P. (2003), Imbalanced weak magnetohydrodynamic turbulence, *Astrophys. J.*, , 582, 1220 - 1240
- Marsch, E., Goertz, C. K., & Richter, K. (1982), Wave heating and acceleration of solar wind ions by cyclotron resonance, *J. Geophys. Res.*, , 87, 5030 - 5044
- Masuda, S., Kosugi, T., Hara, H., Tsuneta, S., & Ogawara, Y. (1994), A Loop-Top Hard X-Ray Source in a Compact Solar Flare as Evidence for Magnetic Reconnection, *Nature*, 371, 495 - 497
- Matthaeus, W. H., Zank, G. P., Oughton, S., Mullan, D. J., & Dmitruk, P. (1999), Coronal heating by magnetohydrodynamic turbulence driven by reflected low-frequency waves, *Astrophys. J.*, , 523, L93 - L96
- Miyagoshi, T., Isobe, T., Yokoyama, T., & Shibata, K. (2005), in preparation
- Moore, R. L., Suess, S. T., Musielak, Z. E., & An, A.-H. (1991), Alfvén wave trapping, network microflaring, and heating in solar coronal holes, *Astrophys. J.*, , 378, 347 - 359
- Moriyasu, S., Kudoh, T., Yokoyama, T., & Shibata, K. (2004), The nonlinear Alfvén wave model for solar coronal heating and nanoflares, *Astrophys. J.*, , 601, L107 - L110
- Nakagawa, T., Gopalswamy, N., & Yashiro, S. (2005), Solar wind speed within $20R_{\odot}$ of the sun estimated from limb CMEs, submitted to *J. Geophys. Res.*,
- Nakariakov, V. M., Roberts, B., & Murawski, K. (1998), Nonlinear coupling of MHD waves in inhomogeneous steady flows, *Astron. Astrophys.*, , 332, 795 - 804, 1998
- Ofman, L. & Davila, J. M. (1998), Solar wind acceleration by large-amplitude nonlinear waves: Parametric study, *J. Geophys. Res.*, , 103, 23677 - 23690
- Ofman, L., Nakariakov, V. M., & Deforest, C. E. (2001), Slow magnetosonic waves in coronal plumes, *Astrophys. J.*, , 514, 441 - 447
- Ofman, L. (2004), Three-fluid model of the heating and acceleration of the fast solar wind, *J. Geophys. Res.*, , 109, A07102
- Orta, J. A., Huerta, M. A., & Boynton, G. C. (2003), Magnetohydrodynamic Shock Heating of the Solar Corona, *Astrophys. J.*, , 596, 646 - 655
- Oughton, S., Matthaeus, W. H., Dmitruk, P., Milano, L. J., Zank, G. P., & Mullan, D. J. (2001), A reduced magnetohydrodynamic model of coronal heating in open magnetic regions driven by reflected low-frequency Alfvén waves, *Astrophys. J.*, , 551, 565 - 575
- Parenti, S., Bromage, B. J. I., Poletto, G., Noci, G., Raymond, J. C., & Bromage, G. E. (2000), Characteristics of solar coronal streamers. Element abundance, temperature and density from coordinated CDS and UVCS SOHO observations, *Astron. Astrophys.*, , 363, 800
- Parnell, C. E. & Jupp, P. E. (2000), Statistical Analysis of the Energy Distribution of Nanoflares in the Quiet Sun, *Astrophys. J.*, , 529, 554 - 569
- Phillips, J. L. et al. (1995), Ulysses solar wind plasma observations from pole to pole. *Geophys. Res. Lett.*, , 22, 3301 - 3304
- Richardson, I. G., Berdichevsky, D., Desch, M. D., & Farrugia, C. J. (2000), Solar-cycle variation of low density solar wind during more than three solar cycles, *Geophys. Res. Lett.*, , 27, 3761 - 3764
- Sakurai, T., Ichimoto, K., Raju, K. P., & Singh, J. (2002), Spectroscopic Observation of Coronal Waves, *Sol. Phys.*, 209, 265 - 286
- Sano, T. & Inutsuka, S. (2005), in preparation
- Schwadron, N. A. & McComas, D. J. (2003), Solar Wind Scaling Law, *Astrophys. J.*, , 599, 1395 - 1403
- Sheeley, N. R. Jr. et al. (1997), Measurements of Flow Speeds in the Corona between 2 and $30 R_{\odot}$, *Astrophys. J.*, , 484, 472
- Smith, C. W., Mullan, D. J., Ness, N. F., Skoug, R. M., & Steinberg, J. (2001), Day the solar wind almost disappeared: Magnetic field fluctuations, wave refraction and dissipation, *J. Geophys. Res.*, , 106, 18625 - 18634
- Sturrock, P. A. (1999), Chromospheric Magnetic Reconnection and Its Possible Relationship to Coronal Heating, *Astrophys. J.*, , 521, 451 - 459
- Suzuki, T. K. (2002), On the Heating of the Solar Corona and the Acceleration of the Low-Speed Solar Wind by Acoustic Waves Generated in the Corona, *Astrophys. J.*, , 578, 598 - 609
- Suzuki, T. K. (2004), Coronal heating and acceleration of the high/low-speed solar wind by fast/slow MHD shock trains, *Mon. Not. R. Astron. Soc.*, , 349, 1227 - 1239
- Suzuki, T. K. & Inutsuka, S. (2005), Making the corona and the fast solar wind: a self-consistent simulation for the low-frequency Alfvén waves from photosphere to 0.3AU, *ApJL*, 632, L49 - L52
- Suzuki, T. K., Yan, H., Lazarian, A., Cassinelli, J. P. (2005), submitted to *Astrophys. J.*,
- Suzuki, T. K., Fujiki, K., Kojima, M., Tokumaru, M., Hakamada, K., Hirano M., Baba, (2005), in preparation
- Terasawa, T., Hoshino, M., Sakai, J. I., & Hada, T. (1986), Decay instability of finite-amplitude circularly polarized Alfvén waves: A numerical simulation of stimulated Brillouin scattering, *J. Geophys. Res.*, , 91, 4171
- Teriaca, L., Poletto, G., Romoli, M., & Biesecker, D. A. (2003), The nascent solar wind: origin and acceleration, *Astrophys. J.*, , 588, 566 - 577
- Thompson, K. W. (1987), Time dependent boundary conditions for hyperbolic systems, *J. Computational. Phys.*, , 68, 1
- Tsiklauri, D., Sakai, J.-T., & Saito, S. (2005), Particle-In-Cell simulations of circularly polarised Alfvén wave phase mixing: A new mechanism for electron acceleration in collisionless plasmas, *Astron. Astrophys.*, , 435, 1105 - 1113

- Tsuneta, S., Hara, H., Shimizu, T., Acton, L. W., Strong, K. T., Hudson, H. S., & Ogawara, Y.(1992), Observation of a solar flare at the limb with the YOHKOH Soft X-ray Telescope, *PASJ*, 44, L63 - L69
- Tsurutani, B. T. & Ho, C. M.(1999), A review of discontinuities and Alfvén waves in interplanetary space: Ulysses results, *Rev. Geophys.*, 37, 517 - 524
- Tsurutani, B. T. et al. (2002), Relationship between discontinuities, magnetic holes, magnetic decreases and nonlinear Alfvén waves: Ulysses observations over the solar poles, *Geophys. Res. Lett.*, , 29, 23-1
- Tsurutani, B. T., Lakhina, G. S., Pickett, J. S., Guarnieri, F. L., Lin, N., & Goldstein, B. E. (2005), Nonlinear Alfvén waves, discontinuities, proton perpendicular acceleration, and magnetic holes/decreases in interplanetary space and the magnetosphere: intermediate shocks?, *Nonlinear Processes in Geophysics*, 21, 321 - 336
- Tu, C. Y. & Marsch, E.(2001), Wave dissipation by ion cyclotron resonance in the solar corona, *Astron. Astrophys.*, , 368, 1071 - 1076
- Tu, C.-Y., Zhou, C., Marsch, E., Xia, L.-D., Zhao, L., Wang, J.-X., & Wilhelm, K.(2005), Solar Wind Origin in Coronal Funnels, *Science*, 308, 519 - 523
- Usmanov, A. V., Goldstein, M. L., & Farrell, W. M.(2000), A view of the inner heliosphere during the May 10-11, 1999 low density anomaly *Geophys. Res. Lett.*, , 27, 3765
- Wang, Y.-M. & Sheeley, Jr, N. R.(1990), Solar wind speed and coronal flux-tube expansion, *Astrophys. J.*, , 355, 726 - 732
- Wang, Y.-M. & Sheeley, Jr, N. R.(1991), Why fast solar wind originates from slowly expanding coronal flux tubes, *Astrophys. J.*, , 372, L45 - L48
- Wang, Y.-M., Sheeley, N. R., Socker, D. G., Howard, R. A., Rich, N. B. (2000), *J. Geophys. Res.*, , 105, 25133
- Wilhelm, K., Marsch, E., Dwivedi, B. N., Hassler, D. M., Lemaire, P., Gabriel, A. H., & Huber, M. C. E. (1998), The solar corona above polar coronal holes as seen by SUMER on SOHO, *Astrophys. J.*, , 500, 1023 - 1038
- Withbroe, G. L. & Noyes, R. W.(1977), Mass and energy flow in the solar chromosphere and corona, *ARA&A*, 15, 363 - 387
- Wu, C. C.(1987), On MHD intermediate shocks, *Geophys. Res. Lett.*, , 14, 668 - 671
- Wu, S. T., Zheng, H., Wang, S., Thompson, B. J., Plunkett, S. P., Zhao, X. P., Dryer, M.(2001), Three-dimensional numerical simulation of MHD waves observed by the Extreme Ultraviolet Imaging Telescope, *J. Geophys. Res.*, , A11, 25089 - 25102
- Yan, H. & Lazarian, A. (2004), Cosmic-Ray Scattering and Streaming in Compressible Magnetohydrodynamic Turbulence, *Astrophys. J.*, , 614, 757-769
- Zangrilli, L., Poletto, G., Nicolosi, P., Noci, G., & Romoli, M.(2002), Two-dimensional structure of a polar coronal hole at solar minimum: new semiempirical methodology for deriving plasma parameters. *Astrophys. J.*, , 574, 477 - 494

Department of Physics, Kyoto University, Kitashirakawa, Kyoto, 606-8502, Japan; stakeru@scphys.kyoto-u.ac.jp

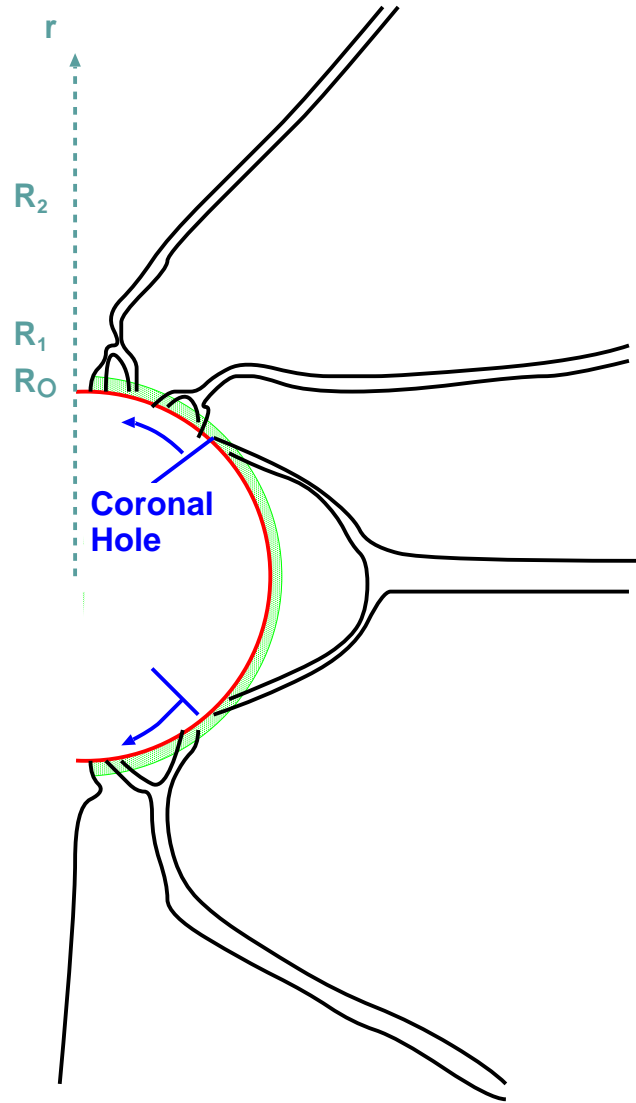


Figure 1. Schematic picture for the geometry of flux tubes. Solid lines indicate magnetic field lines, and dotted line is coordinate of heliocentric distance, r . Shaded region denotes the chromosphere. Our 1D simulations treat each individual flux tube separately. The flux tubes firstly expand at $\sim R_1 (= 1.01R_\odot)$ in our simulations) by closed loops with length $\sim 10^4 \text{ km} (= 0.014R_\odot)$, and then, they expand at $\sim R_1 (= 1.2R_\odot)$ in our simulations) due to the large-scale dipole structure.

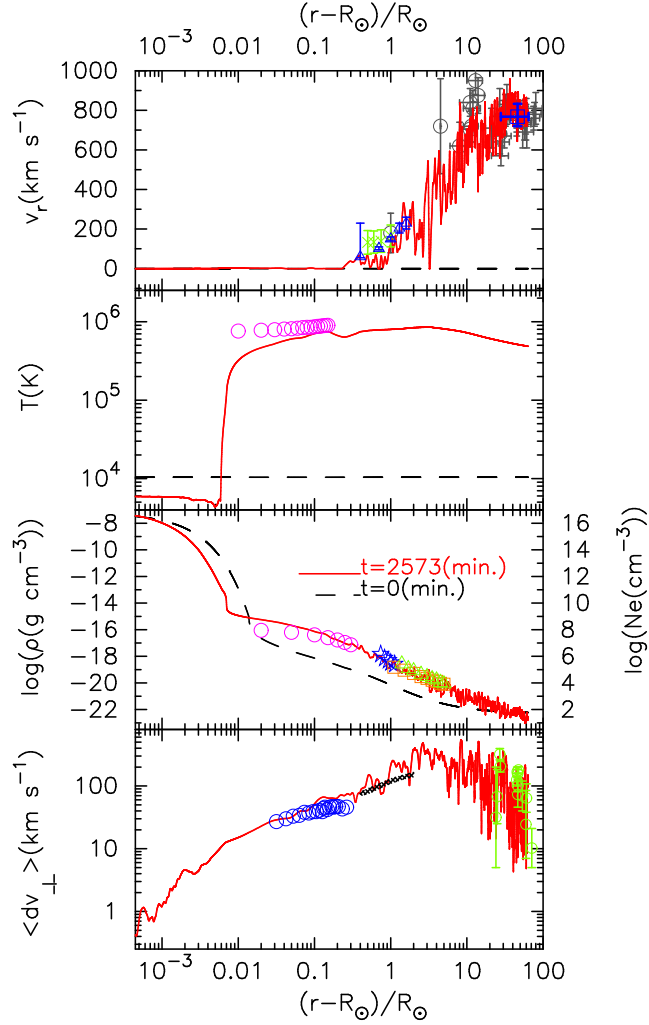


Figure 2. Results of Run I with observations of fast solar wind. From top to bottom, outflow speed, v_r (km s^{-1}), temperature, T (K), density in logarithmic scale, $\log(\rho)$ (g cm^{-3}), and rms transverse amplitude, $\langle dv_{\perp} \rangle$ (km s^{-1}) are plotted. Observational data in the third panel are electron density, $\log(N_e)$ (cm^{-3}) which is to be referred to the right axis. Dashed lines indicate the initial condition and solid lines are the results at $t = 2573$ minutes. In the bottom panel, the initial value ($\langle dv_{\perp} \rangle = 0$) does not appear. *first:* Green vertical error bars are proton outflow speed in interplume region by UVCS/SoHO [Teriaca et al., 2003]. Dark blue vertical error bars are proton outflow speed by Doppler dimming technique using UVCS/SoHO data [Zangrilli et al., 2002]. Dark blue open square with errors is velocity by IPS measurements averaged in 0.13 - 0.3AU of high-latitude regions [Kojima et al., 2004]. Light blue data are taken from Grall et al. [1996]; crossed bars are IPS measurements by EISCAT, crossed bars with open circles are by VLBA measurements, and vertical error bars with open circles are data based on observation by SPARTAN 201-01 [Habbal et al., 1994]. *second:* Pink circles are electron temperature by CDS/SoHO [Fludra et al., 1999]. *third:* Circles and stars are observations by SUMER/SoHO [Wilhelm et al., 1998] and by CDS/SoHO [Teriaca et al., 2003], respectively. Triangles [Teriaca et al., 2003] and squares [Lamy et al., 1997] are observations by LASCO/SoHO. *fourth:* Blue circles are non-thermal broadening inferred from SUMER/SoHO measurements [Banerjee et al., 1998]. Cross hatched region is empirical constraint of non-thermal broadening based on UVCS/SoHO observation [Esser et al., 1999]. Green error bars are transverse velocity fluctuations derived from IPS measurements by EISCAT [Canals et al., 2002].

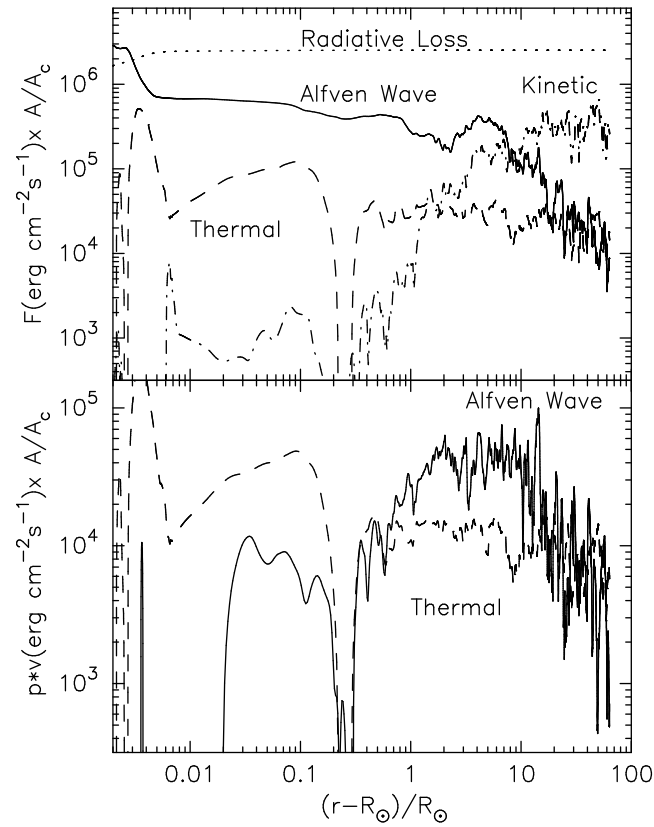


Figure 3. Energy flux (top) and momentum flux (bottom) as a function of distance from the photosphere. Hollows at $r \simeq 1.2 - 1.3R_{\odot}$ in both panels are due to negative v_r there. *top:* Solid, dashed, dot-dashed, and dotted lines denote the energy flux of the Alfvén wave, the enthalpy flux, the kinetic energy flux, and the integrated radiative loss. *bottom* Solid and dashed lines indicate the advected pressure terms of the Alfvén waves, $\langle p_A v_r \rangle$ and the thermal pressure, $\langle p v_r \rangle$.

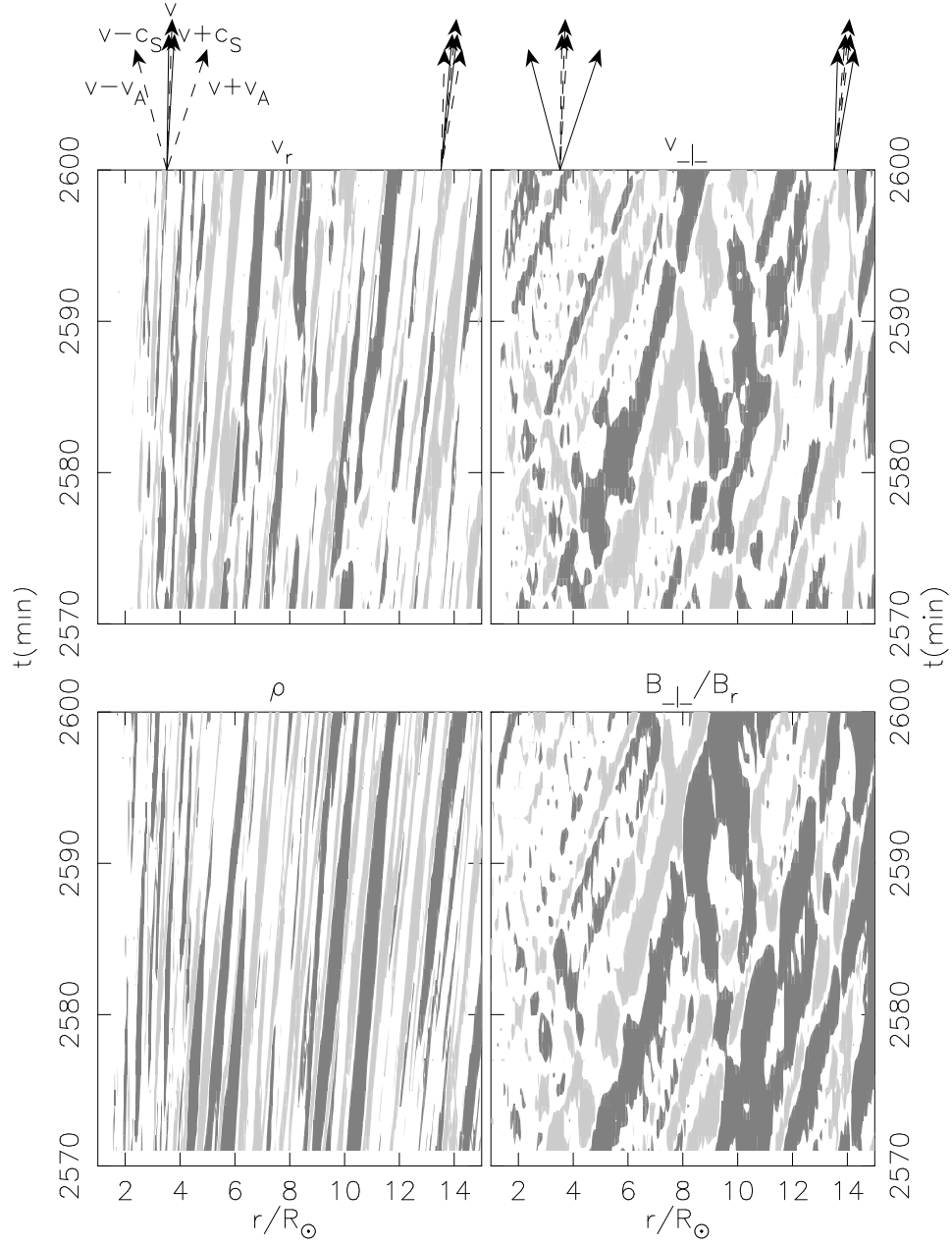


Figure 4. $r - t$ diagrams for v_r (upper-left), ρ (lower-left), v_{\perp} (upper-right), and B_{\perp}/B_r (lower-right.) The horizontal axes cover from R_{\odot} to $15R_{\odot}$, and the vertical axes cover from $t = 2570$ minutes to 2600 minutes. Dark and light shaded regions indicate positive and negative amplitudes which exceed certain thresholds. The thresholds are $dv_r = \pm 96 \text{ km/s}$ for v_r , $d\rho/\rho = \pm 0.25$ for ρ , $v_{\perp} = \pm 180 \text{ km/s}$ for v_{\perp} , and $B_{\perp}/B_r = \pm 0.16$ for B_{\perp}/B_r , where $d\rho$ and dv_r are differences from the averaged ρ and v_r .

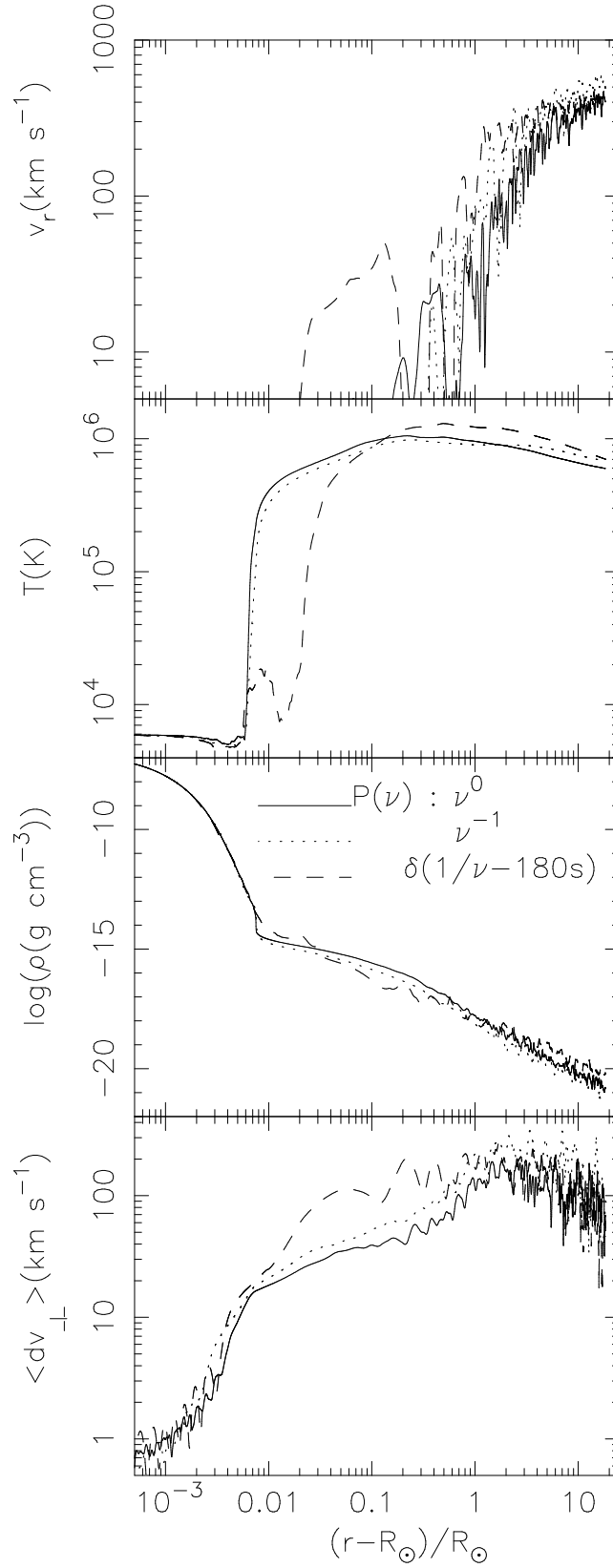


Figure 5. Structures of corona and solar wind for various fluctuation spectra at the photosphere. From top to bottom, solar wind speed, v_r (km s^{-1}), temperature, T (K), density in logarithmic scale, $\log(\rho(\text{g cm}^{-3}))$, and rms transverse velocity, $\langle dv_{\perp} \rangle$ (km s^{-1}). Dotted, solid, and dashed lines are results of $P(\nu) \propto \nu^{-1}$ (Run II), ν^0 (Run III), and $\delta(1/\nu - 180\text{s})$ (Run IV), respectively.

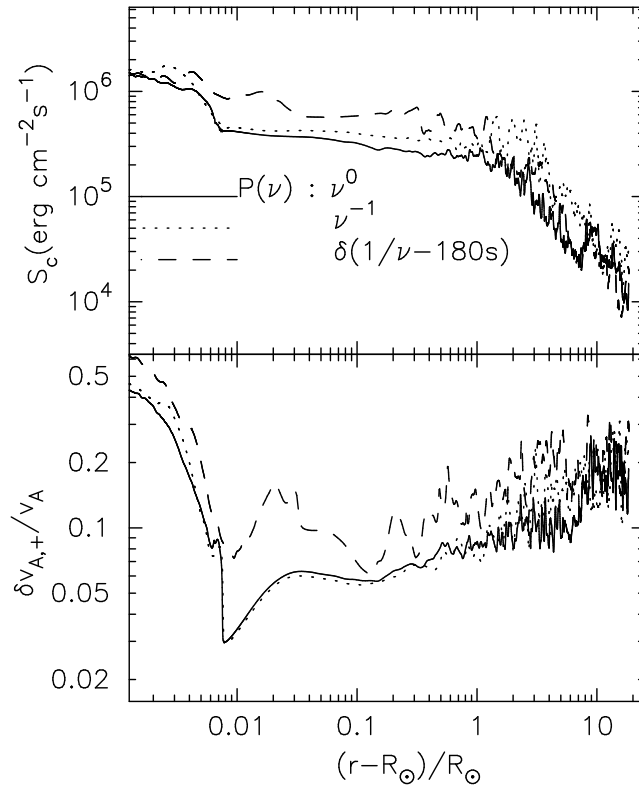


Figure 6. Adiabatic constant, $S_c (\text{erg cm}^{-2} \text{s}^{-1})$, (top) and normalized amplitude, $\delta v_{A,+} / v_A$, (bottom) of outgoing Alfvén waves for various spectrums. Dotted, solid, and dashed lines are results of $P(\nu) \propto \nu^{-1}$ (Run II), ν^0 (Run III), and $\delta(1/\nu - 180\text{s})$ (Run IV), respectively.

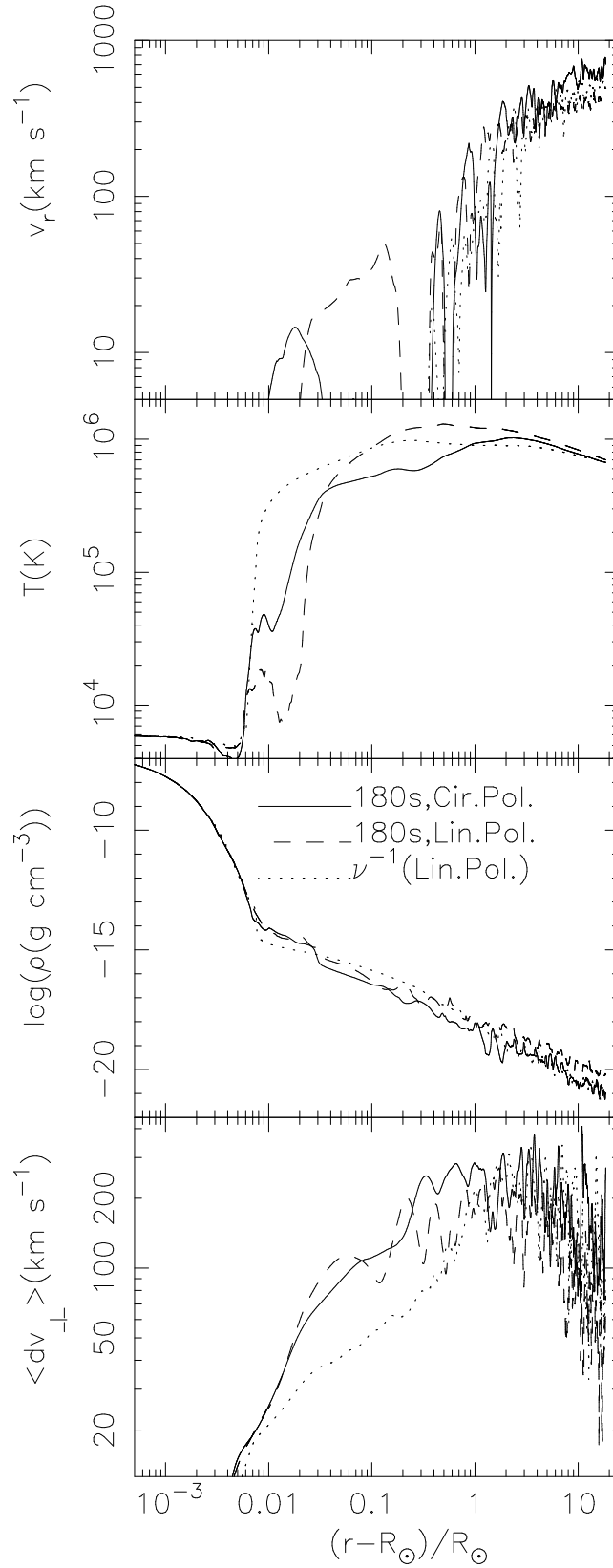


Figure 7. Same as Figure 5 but for different polarizations of the perturbations. Solid, dashed, and dotted lines are results of circular polarized sinusoidal waves (Run V), linearly polarized sinusoidal waves (Run IV), and linearly polarized waves with power spectrum, $P(\nu) \propto \nu^{-1}$ (Run II), respectively.

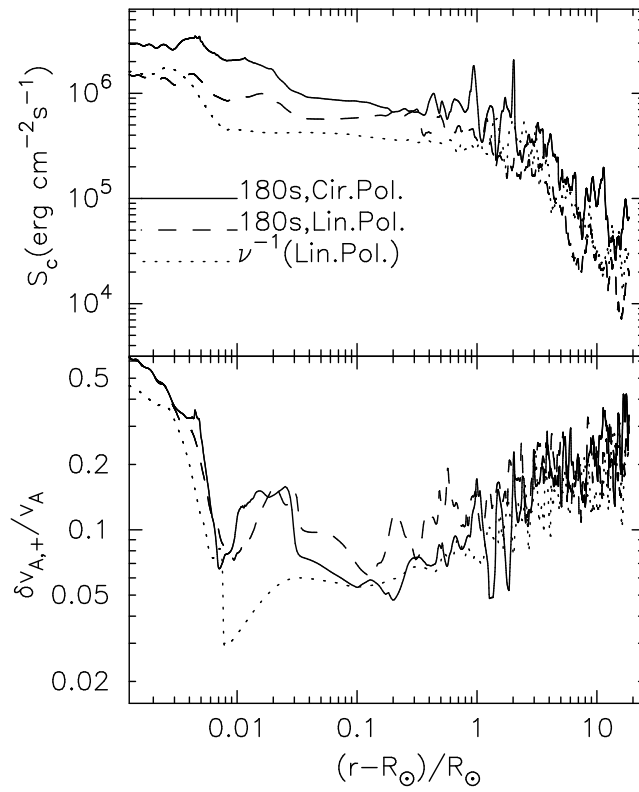


Figure 8. Same as Figure 6 but for different polarizations of the perturbations. Solid, dashed, and dotted lines are results of circular polarized sinusoidal waves (Run V), linearly polarized sinusoidal waves (Run IV), and linearly polarized waves with power spectrum, $P(\nu) \propto \nu^{-1}$ (Run II), respectively.

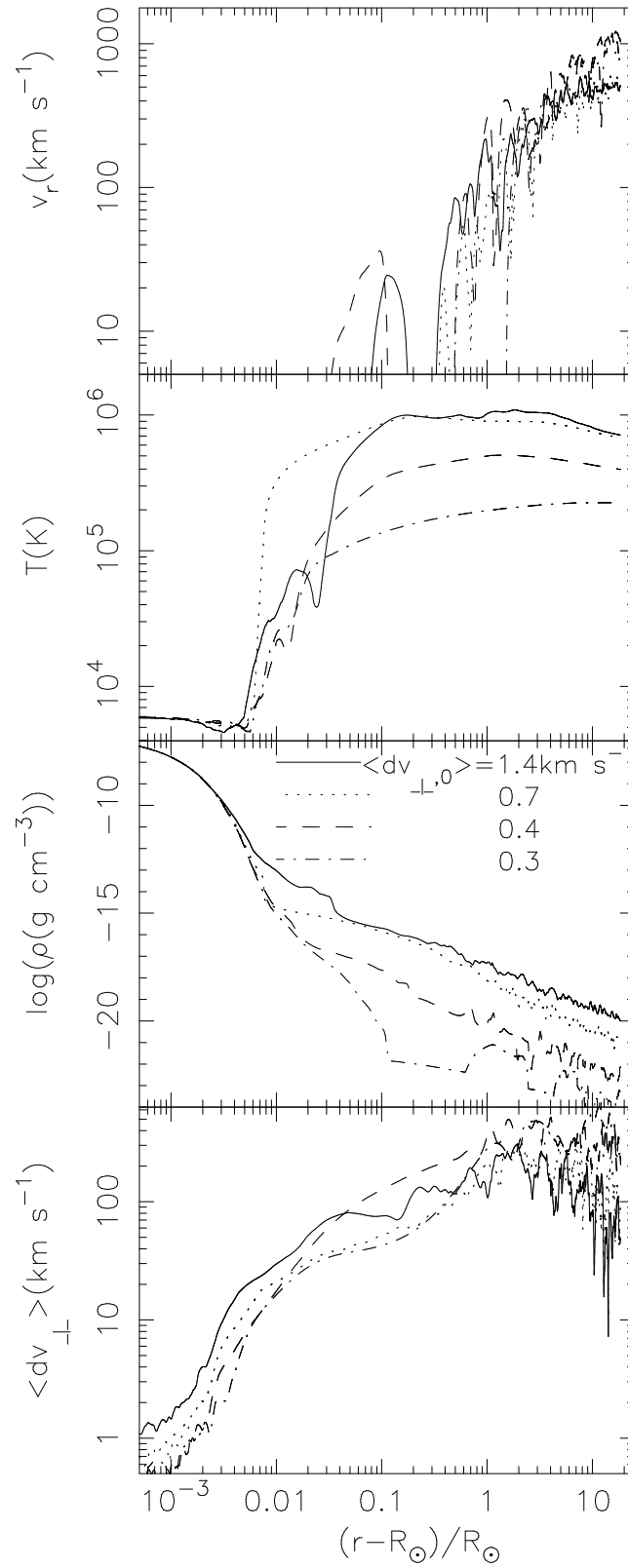


Figure 9. Same as Figure 5 but for different $\langle dv_{\perp,0} \rangle$. Solid, dotted, dashed, and dot-dashed lines are results of $\langle dv_{\perp,0} \rangle = 1.4$ (Run VI), 0.7 (Run II), 0.4 (Run VII), and $0.3(\text{km s}^{-1})$ (Run IX), respectively.

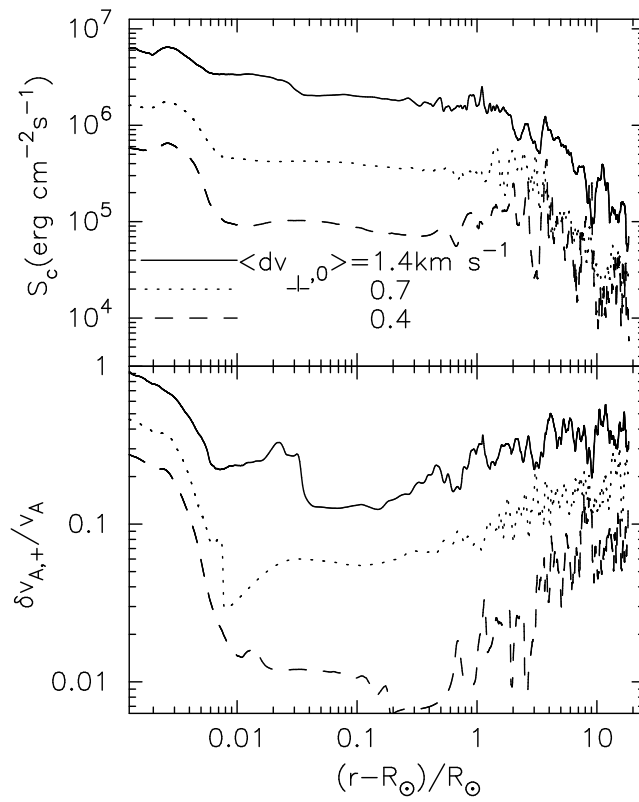


Figure 10. Same as Figure 6 but for different $\langle dv_{\perp,0} \rangle$. Solid, dotted, and dashed lines are results of $\langle dv_{\perp,0} \rangle = 1.4$ (Run VI), 0.7 (Run II), and $0.4(\text{km s}^{-1})$ (Run VII), respectively.

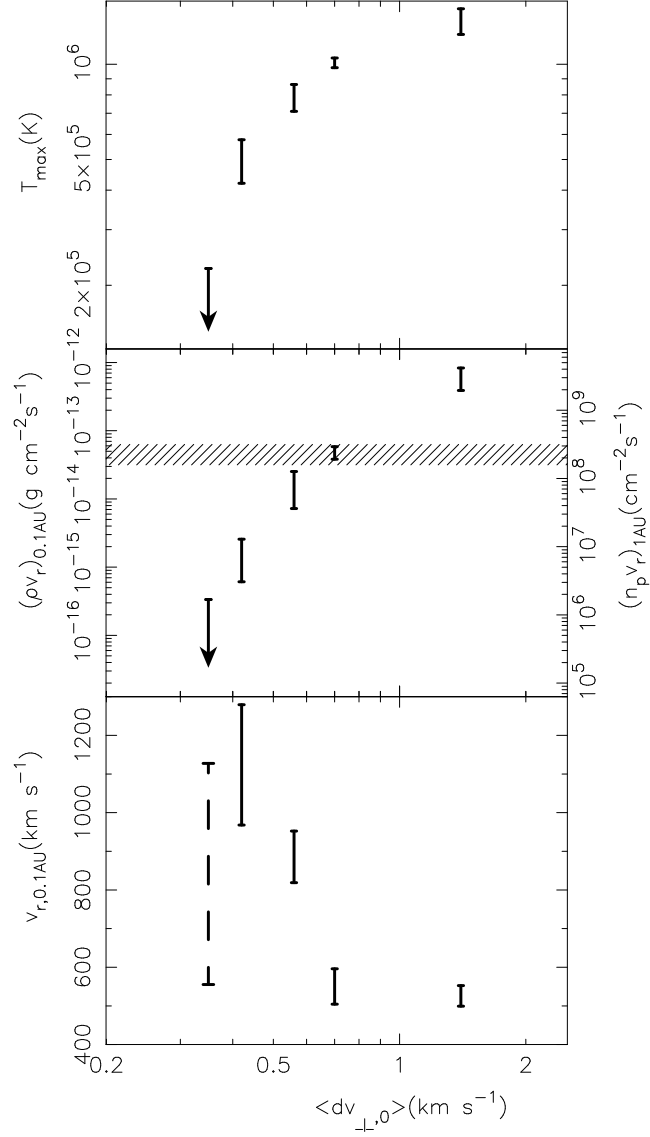


Figure 11. The maximum temperature, T_{\max} (K), (top), the mass flux of solar wind at 0.1AU, $(\rho v_r)_{0.1\text{AU}}$ (g cm⁻²s⁻¹), (middle), and the solar wind speed at 0.1AU, $v_{r,0.1\text{AU}}$ (km s⁻¹) (bottom). On the right axis of the middle panel, we show proton flux at 1AU, $(n_p v_r)_{1\text{AU}}$ (cm⁻² s⁻¹) estimated by assuming mean molecular weight of 0.6. Shaded region in the middle panel is observed proton flux at 1AU. Upper limits in the top and middle panels for $\langle dv_{\perp,0} \rangle = 0.3\text{km s}^{-1}$ indicates that stable corona with the sufficient mass supply cannot be maintained and both T_{\max} and $(\rho v_r)_{0.1\text{AU}}$ decreases as the simulation proceeds. The wind speed also varies a lot, hence, the dashed error bar is used only for that case.

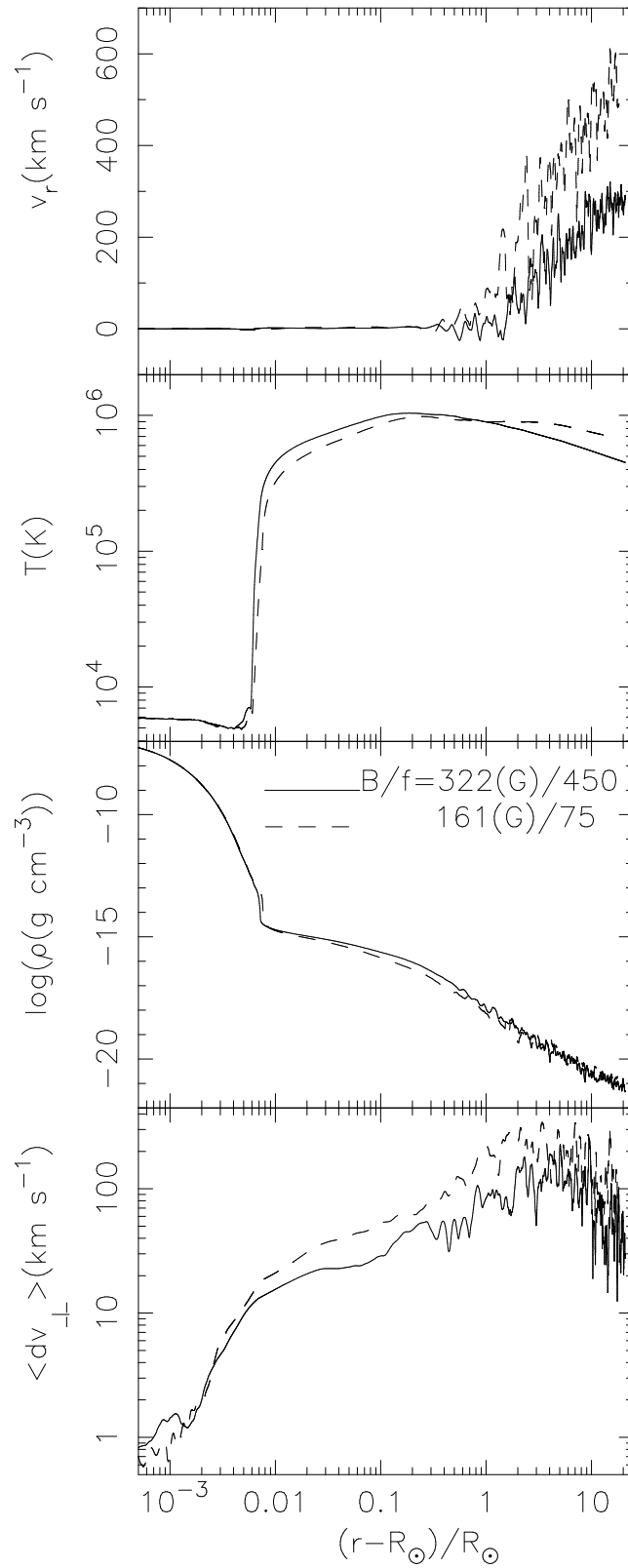


Figure 12. Same as Figure 5 but for different $B_{r,0}/f_{\max}$. Solid and dashed lines are results of $B_{r,0}(\text{G})/f_{\max} = 322/450$ (Run VIII) and $161/75$ (Run II), respectively.

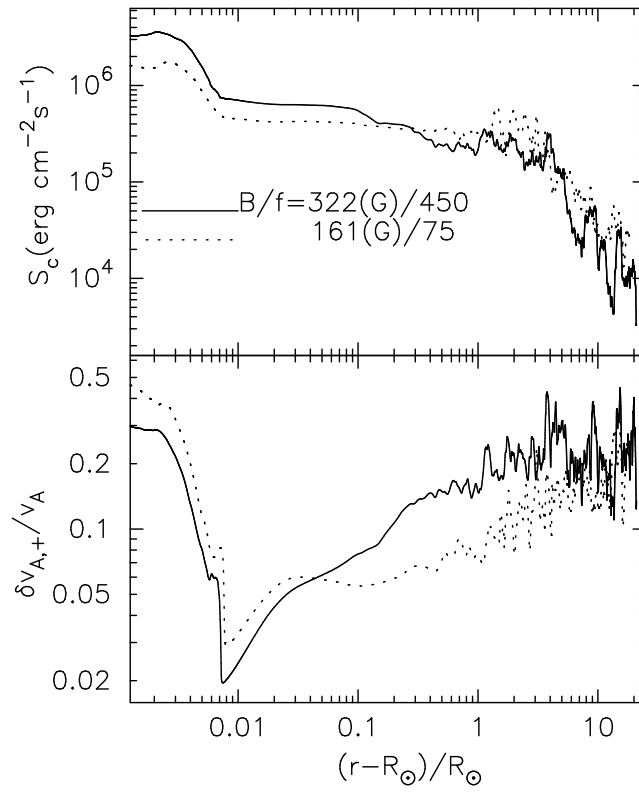


Figure 13. Same as Figure 6 but for different $B_{r,0}/f_{\max}$. Solid and dashed lines are results of $B_{r,0}(\text{G})/f_{\max} = 322/450$ (Run VIII) and $161/75$ (Run II), respectively.

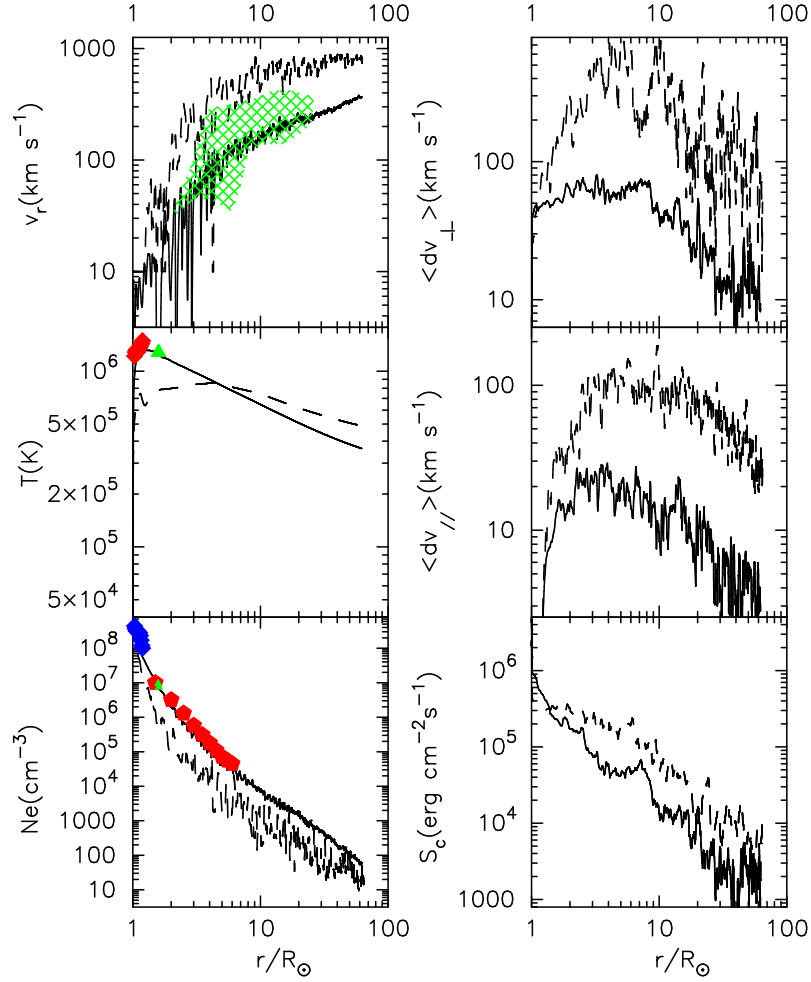


Figure 14. Simulation results of the slow (Run X; solid lines) and fast (Run I; dashed lines) solar winds in comparison with slow-wind observations. On the left from top to bottom, the outflow velocity, v_r (km s^{-1}), temperature, T (K), and electron density, N_e (cm^{-3}), are plotted with observation of mid- to low-latitude regions where the slow winds come from. (see Figure 2 for the fast-wind observations). On the right from top to bottom rms transverse velocity, $\langle dv_{\perp} \rangle$ (km s^{-1}), rms longitudinal velocity, $\langle dv_{\parallel} \rangle$ (km s^{-1}), and the adiabatic constant, S_c ($\text{erg cm}^{-2} \text{s}^{-1}$) of the outgoing Alfvén waves are plotted. *Observational data; top-left* : Shaded region is observational data in the streamer belt [Sheeley et al., 1997]. *Middle-left* : Filled diamonds and triangles are electron temperature obtained from the line ratio of Fe XIII/X in the mid-latitude streamer by CDS/SOHO and UVCS/SOHO respectively [Parenti et al., 2000] *bottom-left* : Filled diamonds and triangles are data respectively from CDS and UVCS on SOHO observation of the mid-latitude streamer [Parenti et al., 2000], and filled pentagons derived from observation of the total brightness in the equator region by LASCO/SOHO [Hayes et al., 2001].

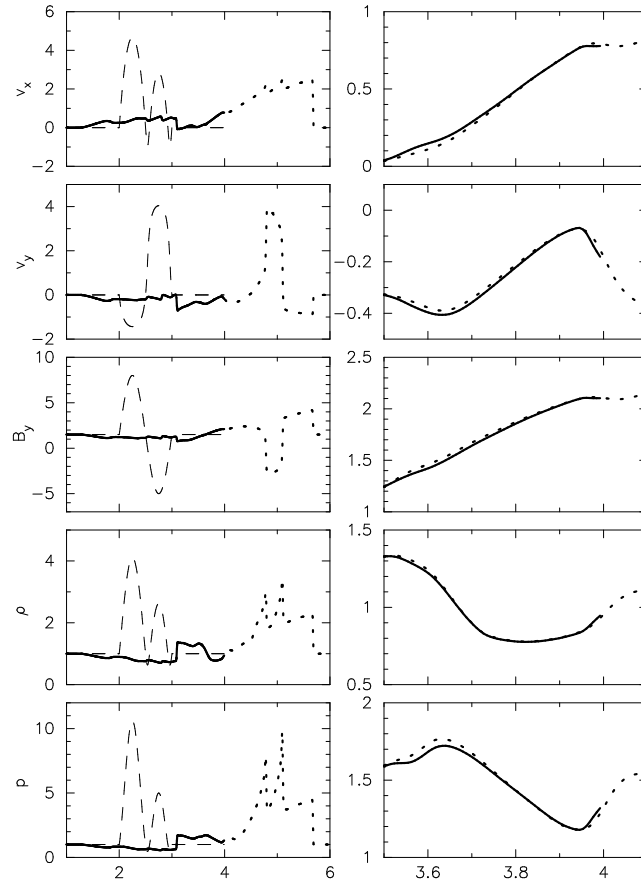


Figure 15. Reflection test for the oblique simple fast wave with $\delta v/v_f = 3.1$. From top to bottom, v_x , v_y , B_y , ρ , and p are plotted. In the panels on the right each quantity on the left is zoomed-up. Solid and dashed lines denotes the initial and final ($t = 0.6$) states. Dotted lines are results of simulation in the broader region at $t = 0.6$. Differences between solid and dotted lines indicate errors due to our implementation of the outgoing boundary condition.

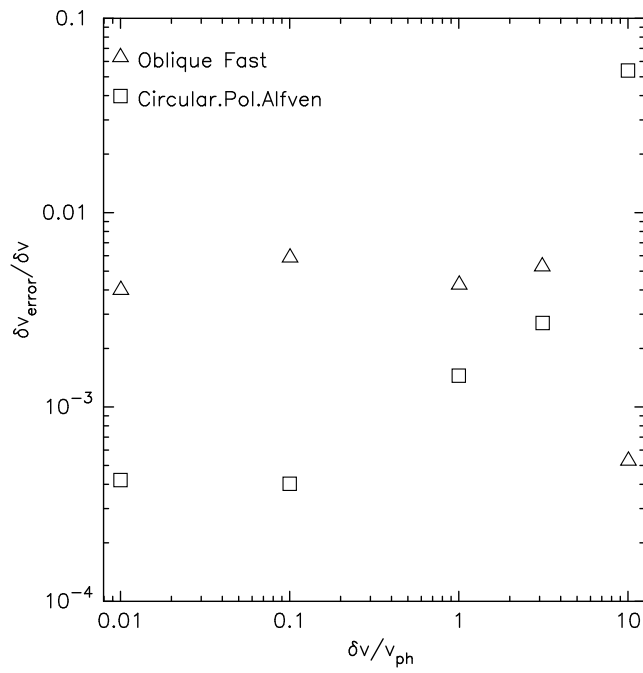


Figure 16. Reflection test for the simple fast and the Alfvén waves. Horizontal axis shows the input wave amplitudes normalized by the phase speed. Vertical axis plots errors due to our implementation of the outgoing boundary condition normalized by the input amplitude. (see text)